Utilization of O_4 slant column density to derive aerosol layer height from a spaceborne UV-Visible hyperspectral sensor: Sensitivity and case study

Sang Seo Park[1], Jhoon Kim[1,*], Hanlim Lee[1,2], Omar Torres[3], Kwang-Mog Lee[4], Sang Deok Lee[5]

[1]Department of Atmospheric Science, Yonsei University, Seoul, Korea.

[2]Department of Spatial Information Engineering, Pukyong National University, Busan, Korea

[3]NASA Goddard Space Flight Center, Greenbelt, Maryland, United States

[4]Department of Astronomy and Atmospheric Science, Kyungpook National University, Daegu, Korea

[5]National Institute of Environment Research, Ministry of Environment, Incheon, Korea

* Correspondence to: Jhoon Kim (jkim2@yonsei.ac.kr)

Tel. : +82-2-2123-5682, Fax: +82-2-365-5163

Abstract

The sensitivities of oxygen-dimer (O_4) slant column densities (SCDs) to changes in aerosol layer height are investigated using the simulated radiances by a radiative transfer model, the Linearlized pseudo-spherical vector discrete ordinate radiative transfer (VLIDORT), and the Differential Optical Absorption Spectroscopy (DOAS) technique. The sensitivities of the O4 index (O4I), which is defined as O_4 SCD divided by 10^{40} molecules^{2}cm^{-5}, to aerosol types and optical properties are also evaluated and compared. Among the O_4 absorption bands at 340, 360, 380, and 477 nm, the O_4 absorption band at 477 nm is found to be the most suitable to retrieve the aerosol effective height. However, the O4I at 477 nm is significantly influenced not only by the aerosol layer effective height but also by aerosol vertical profiles, optical properties including single scattering albedo (SSA), aerosol optical depth (AOD), particle size, and surface albedo. Overall, the error of the retrieved aerosol effective height is estimated to be 1276, 846, and 739 m for dust, non-absorbing, and absorbing aerosol, respectively, assuming knowledge on the aerosol vertical distribution shape. Using radiance data from the Ozone Monitoring Instrument (OMI), a new algorithm is developed to derive the aerosol effective height over East Asia after the determination of the aerosol type and AOD from the MODerate resolution Imaging Spectroradiometer (MODIS). About 80% of retrieved aerosol effective heights are within the error range of 1 km compared to those obtained from the Cloud-Aerosol Lidar with Orthogonal Polarization (CALIOP) measurements on thick aerosol layer cases.

1. Introduction

Aerosol is one of the key atmospheric constituents in understanding climate changes with its effects on direct and diffuse solar radiation (e.g., Haywood and Shine, 1995; Kaufman *et al.*, 2002), and plays an important role in air quality near the surface (e.g., Watson *et al.*, 1994; Prospero, 1999). For these reasons, observations from satellite remote sensing have been carried out to investigate aerosol properties at regional and global scale, including aerosol optical depth (AOD) (e.g., Curier *et al.*, 2008; Levy *et al.*, 2007; Torres *et al.,* 2007; Ahn *et al.*, 2014; Veefkind *et al.*, 1999; Zhang *et al.*, 2011), fine mode fraction (FMF) or Angstrom Exponent (AE) (e.g., Jones and Christopher, 2007; Lee *et al.*, 2010; Nakajima and Higurashi, 1998; Remer *et al.*, 2008), single scattering albedo (SSA) (e.g., Dubovik *et al.*, 2002; Levy *et al.*, 2007; Jeong and Hsu, 2008; Torres *et al.*, 1998, 2005, 2007; Jethva *et al.*, 2014), and aerosol types (e.g., Higurashi and Nakajima, 2002; Kim *et al.*, 2007; Lee *et al.*, 2010). These information were further utilized to estimate radiative forcing of aerosol (e.g., Christopher *et al.*, 2006; Chung *et al.*, 2005; Chou *et al.*, 2002), to understand the mechanism of the changes to the cloud formation (Twomey *et al.,* 1984; Albrecht, 1989; Jones *et al.,* 1994), and to monitor air quality (e.g., Wang and Christopher, 2003; Hutchison *et al.,* 2005).

Vertical profiles of atmospheric aerosols are affected by processes of formation, transport and deposition, and vary for different aerosol types over East Asia (Shimizu *et al.*, 2004). Labonne *et al.* (2007) also reported that the layer top height of biomass burning aerosol ranged from 1.5 to 7 km in the wild fire regions. The information on the aerosol layer height is important, because the variation of the aerosol vertical distribution affects radiative process in the atmosphere near the surface and trace gas

retrieval for air mass factor calculation. Uncertainty in aerosol layer height also affects the accuracy of aerosol AOD and SSA retrieval algorithms that use near UV observations (Torres *et al.*, 1998; Torres *et al.*, 2007; Jethva *et al.*, 2014) and complicates the interpretation of the Aerosol Index (AI), a qualitative parameter commonly used to detect absorbing aerosols (Herman *et al.*, 1997; Torres *et al.,* 1998). In addition, there have been difficulties to estimate surface concentration of aerosol from AODs, because the information on aerosol vertical distribution is not readily available and even hard to predict from the state-of-the-art models due to its large variability. Although the Cloud-Aerosol Lidar with Orthogonal Polarization (CALIOP) has been successful and provided vertical profiles of aerosols, its spatial coverage was very limited with its measurement characteristics (Omar *et al.*, 2009). Liu *et al.* (2005) showed that the Particulate Matter (PM) concentration estimated by the AOD from satellite observation accounted for only 48% of the measured surface PM, although their study reflected variations of the aerosol types and its hygroscopic growth in the algorithms. One of the essential factors to consider in estimating PM from AOD is the vertical structure of aerosols (e.g. Chu, 2006; Seo *et al.*, 2015). Therefore, conventional aerosol products would benefit significantly with the development of robust algorithm to retrieve aerosol height using satellite data.

The Differential Optical Absorption Spectroscopy (DOAS) technique has been used widely to retrieve trace gas concentration both from ground-based (e.g., Platt, 1994; Platt and Stutz, 2008) and space-borne (e.g., Wagner et al., 2007; Wagner *et al*., 2010) measurements. After the work of Platt (1994) to retrieve trace gas concentration by using DOAS, Wagner et al. (2004) suggested to derive atmospheric aerosol information from O_4 measurement by using Multi Axis Differential Optical Absorption

90 Spectroscopy (MAX-DOAS). Friess et al. (2006) analyzed the model studies to
91 calculate the achievable precision of the aerosol optical depth and vertical profile. In
92 addition, several studies (e.g., Irie *et al.*, 2009 and 2011; Lee *et al.*, 2009 and 2011;
93 Clemer *et al.*, 2010; Li *et al.*, 2010) provided aerosol profiles from ground-based
94 hyperspectral measurements in UV and visible wavelength ranges on several ground
95 sites. Wagner *et al.* (2010) investigated the sensitivity of various factors to the aerosol
96 layer height using the data obtained from the SCanning Imaging Absorption
97 SpectroMeter for Atmospheric ChartographY (SCIAMACHY) on ENVISAT. The
98 sensitivity of the Ring effect and the absorption by oxygen molecule (O_2) and its dimer
99 (O_4) calculated by DOAS method were examined to estimate aerosol properties
100 including the layer height. Kokhanovsky and Rozanov (2010) estimated dust altitudes
101 using the O_2-A band between 760 and 765 nm after the determination of the dust
102 optical depth. In addition, several previous studies are also investigated estimation
103 methods for aerosol height information by using hyperspectral measurement in visible
104 (e.g., Dubuisson *et al.*, 2009; Koppers and Murtagh, 1997; Sanders and de Haan, 2013;
105 Sanghavi *et al.*, 2012; Wang *et al.*, 2012). Because in the near UV the surface signal is
106 significantly smaller than the aerosol signal, the UV and near UV regions are useful to
107 derive aerosol height information from space borne measurements.

108 For OMI measurement, the O_4 band at 477 nm has been widely applied to
109 estimate cloud information (e.g., Accarreta *et al.*, 2004; Sneep *et al.*, 2008). Especially,
110 the cloud information retrieved by O_4 band at 477 nm was used for air mass factor
111 (AMF) analysis with the consideration of aerosol optical effects for the NO_2 column
112 retrieval (e.g., Castellanos et al., 2015, Chimot et al., 2015; Lin et al., 2014; Lin et al.,
113 2015). Although O_4 absorption band around 477 nm varies also due to cloud existence,

it can be also used for the aerosol optical parameter estimation. Veihelmann *et al.* (2007) introduced that the 477 nm channel, which locates major O_4 band, significantly adds degree of freedom for aerosol retrieval by using principal component analysis, and Dirksen *et al.* (2009) adopts the pressure information obtained from OMI O_4 band to identify a plume height for aerosol transport cases.

In this study, the sensitivities of the O_4 bands at 340, 360, 380, and 477 nm to changes in aerosol layer height and its optical properties are estimated using simulated hyperspectral radiances, differently from the previous studies using the O_2-A band observation (e.g., Kokhanovsky and Rozanov, 2010). We proposed an improved DOAS algorithm for the O_4 absorption bands to retrieve aerosol height information from the O_4 slant column densities (SCDs) based on the sensitivity studies. This new algorithm is applied to the radiance data from the Ozone Monitoring Instrument (OMI) to retrieve the aerosol effective height (AEH) for a real case over East Asia, including error estimates.

2. Methods

In general, scattering by aerosol at low altitudes leads to an increase in the length of the average light path (albedo effect), while those at high altitudes causes a decrease in the length of the average light path (shielding effect) (Wagner *et al.*, 2010). These two opposing effects change the estimated O_4 SCD values. Furthermore, the measured O_4 SCD is a function of wavelength, because the absorption and scattering by atmospheric molecules and aerosol have spectral dependence. Therefore, radiative transfer calculations are carried out to estimate the sensitivity of the O_4 SCD with respect to the change of atmospheric conditions. Details of the radiative transfer model

(RTM) and input parameters to simulate radiance are discussed in section 2.1. Analytical method of the DOAS to estimate the O_4 is described in section 2.2.

2.1. Simulation of hyperspectral radiance

Figure 1 shows the flowchart of the method to estimate the O_4 SCD from the simulated radiance. Because the magnitude of the O_4 SCD values is too large to express the sensitivity results, this paper defines the O_4 index (O4I) which is O_4 SCD divided by 10^{40} molecules^{2}cm^{-5}. In order to investigate the sensitivities of the O4I at several bands in UV and visible wavelengths with respect to various aerosol properties, including AEHs, aerosol amounts and aerosol types, the hyperspectral radiance is simulated using the Linearlized pseudo-spherical vector discrete ordinate radiative transfer (VLIDORT) model (Spurr, 2006). The VLIDORT model is based on the linearized discrete ordinate radiative transfer model (LIDORT) (Spurr et al., 2001; Spurr, 2002). This RTM is suitable for the off-nadir satellite viewing geometry of passive sensors since this model adopts the spherically curved atmosphere to reflect the pseudo-spherical direct-beam attenuation effect (Spurr *et al.*, 2001). The model calculates the monochromatic radiance ranging from 300 to 500 nm with a spectral resolution of 0.1 nm. The radiance spectrum is calculated with a 0.2 nm sampling resolution applying a slit response function (SRF) given by a normalized Gaussian distribution with 0.6 nm as the full-width half maximum (FWHM).

2.1.1. Aerosol properties

The aerosol input parameters for the RTM are important in simulating the radiance spectra because aerosol optical properties determine scattering and absorption

characteristics. The data from the Optical Properties of Aerosol and Cloud (OPAC) package (Hess *et al.*, 1998) are used as aerosol parameters, which includes the spectral complex refractive indices and size distribution of aerosols, to calculate SSA and phase function through the Mie calculations. The information of the aerosol parameters are not available at the UV wavelengths, since the AERONET observation provides the information of those aerosol parameters in the visible.

In terms of the aerosol types, water soluble (WASO), mineral dust (MITR), and continental polluted (COPO) model to simulate non-absorbing aerosol, mineral dust, and absorbing anthropogenic aerosol, respectively. The COPO is combined type that includes both soot and WASO, which represents the pure black-carbon and non-absorbing aerosols, respectively. The mixture of these two types, adequately describes the fine mode aerosol from anthropogenic pollution. The SSA is the largest for WASO and the smallest for COPO. In order to account for hygroscopic growth, the default relative humidity is assumed to be 80 % (c.f., Holzer-Popp and Schroedter-Homscheidt, 2004).

2.1.2. Aerosol vertical distribution

In this present study, 'aerosol height' refers to aerosol effective height (AEH), defined as the peak height in Gaussian distribution. According to Hayasaka *et al.* (2007), however, the aerosol extinction coefficient was found to exponentially decrease with altitude over East Asia based on the ground-based LIDAR observation data during the Atmospheric Brown Clouds-East Asia Regional Experiment 2005 (ABC-EAREX 2005) campaign. Previous studies used the exponentially decreasing pattern with altitude to represent the aerosol vertical profiles (e.g. Hayasaka *et al.*,

2007; Li *et al.*, 2010), and reported that aerosol is present within 5 km in altitude for most of the cases (e.g. Sasano, 1996; Chiang *et al.*, 2007). On the other hands, the aerosol vertical distribution does not always follow exponential profile. For the long-range transported aerosol such as dust cases, the aerosol layer profile is quite different than exponential profile and occasionally transported to well above the boundary layer (e.g., Reid et al., 2002; Johnson et al., 2008). The peak height of aerosol extinction profile in long-range transport cases was reported to be located between 1 and 3 km during the Dust and Biomass-burning Aerosol Experiment (DABEX) campaign (Johnson et al., 2008). From these previous studies, standard aerosol vertical profile is difficult to determine. For algorithm development, previous studies assumed that the vertical distribution is assumed to be Gaussian function defined by peak height and half width as representative parameters (Torres et al., 1998; Torres et al., 2005). To supplement the simplicity of assumption for aerosol vertical distribution, aerosol vertical distributions are assumed to be quasi-Gaussian generalized distribution function (GDF), which is Gaussian distribution with dependence on aerosol peak height, width, and layer top and bottom height. Details of GDF can be found in Spurr and Christi (2014) and Yang et al. (2010). In this study, AEH ranges from 1 to 5 km with 1 km width as 1-sigma for the RTM simulation.

2.1.3. Atmospheric gases

The vertical distribution of the O_4 number density, which is used to calculate its SCD from the RTM, is assumed to be the square of the O_2 number density in each layer (Hermans *et al.*, 2003). Thus, the total number of the O_4 column density from surface to TOA is 1.38×10^{43} molecule^{2}cm^{-5}, where 93% and 73% of the total O_4 is

distributed below the altitude of 10 km and 5 km, respectively. In particular, signals by the changes of O_4 are strong below 5 km, where aerosol transports are observed frequently. The vertical distributions of other atmospheric components are taken from the US standard atmosphere 1976 (United States Committee on Extension to the Standard Atmosphere, 1976). The vertical distribution of trace gases and aerosol in the troposphere are interpolated in the 0.1 km resolution from the sea level to 5 km.

2.2. DOAS analysis for O4I estimation

Table 1 summarizes the absorption cross sections of trace gases used as inputs for the radiance simulations and the DOAS spectral analysis. At wavelengths of 340, 360, 380, and 477 nm, the O_4 absorption cross section from Hermans *et al.* (1999) is used in this study. O_3 absorption cross sections at three different temperatures (223, 243, and 273 K) and NO_2 absorption cross sections at two different temperatures (220 and 294 K) are used to account for the amounts in the stratosphere and the troposphere. The radiance information obtained from the RTM simulation is analyzed to derive the O_4 SCDs using WinDOAS software (Van Roozendael and Fayt, 2001) before O4I estimation. To analyze the simulated radiances, the spectrum calculated without all atmospheric gases and aerosol are used as the Fraunhofer reference spectrum (FRS). The simulated spectra are fitted simultaneously with the absorption cross sections of all trace gases listed in Table 1 and FRS in the respective wavelength range of 335-350, 350-370, 370-390, and 460-486 nm, using a nonlinear least squares method (Platt and Stutz, 2008).

On the other hand, the O4I from OMI standard product of cloud (OMCLDO2) (e.g., Accarreta et al., 2004; Sneep et al., 2008) is used to adopt the AEH retrieval on

234 case study. The OMCLDO2 basically used the cross section database from Newnham
235 and Ballard (1998) considering the temperature dependence by interpolating to
236 representative atmospheric temperature of 253 K (Accarreta et al., 2004). For this
237 reason, the O4I from OMCLDO2 and direct estimation from the observed radiance
238 spectra in this present study are possible to have a systematic difference. Figure 2
239 shows the O_4 SCD from OMCLDO2 and those directly retrieved from radiance
240 spectrum over all observed OMI pixels on March 31, 2007 over East Asia. Similar to
241 the DOAS analysis using the simulated spectra, OMI observed radiance spectra are
242 fitted with the Ring spectrum and the FRS in addition to the absorption cross sections
243 in Table 1 within the same wavelength intervals. Before the spectral fitting, the NO_2
244 and O_3 cross sections are I_0 corrected, and the Ring spectrum (Fish and Jones, 1995),
245 accounting for the effects of the rotational Raman scattering due to air molecules, is
246 calculated using the WinDOAS software (Van Roozendael and Fayt, 2001). After the
247 fitting, the noise level of residual spectrum is estimated to be on the order of 10^{-3} for
248 the radiance spectrum at 477 nm from OMI measurements. The O_4 SCDs with the
249 fitting error less than 1% is used for the comparison. From this figure, a systematic
250 difference between two different fitting results is less than 1%, although the cross
251 section databases for fitting are different. From this result, effects of cross section
252 database difference are negligible when the same observation data was used.

253 Figure 3 shows the comparison of the O_4 SCD at 477 nm from a look-up table
254 (LUT) with the dimension as in Table 2 against OMCLDO2 for aerosol and cloud free
255 pixels in year 2005. The clear sky region is selected for the Pacific Ocean with cloud
256 fraction less than 0.02 from OMI observation. The surface albedo is assumed to be
257 0.05, which is similar to the minimum Lambertian equivalent reflectance (LER) over

clear ocean surface (e.g., Kleipool et al., 2008). Because the standard product of the O_4 SCD is only estimated at the 477 nm band, the results can be compared only at this band. To minimize the DOAS fitting error, the observed data from OMI is selected by the fitting precision less than 2% and the quality flags for spectral fitting and pixel condition are also considered. As shown in Figure 3(a), the correlation coefficient of determination (R^2) is 0.864 with a slope of 1.050, and the LUT exhibits a ratio of 0.86±0.05 to the values obtained from OMI standard values. Despite the statistically significant R^2 and slope values between the two values, there exists negative bias by about 14%.

The bias between the retrieved from LUT and estimated from standard product values can be attributed to the differences in the O_4 cross section data and the lack of their temperature and pressure dependence as noted from the previous works by Wagner *et al.* (2009), Clemer *et al.* (2010), and Irie et al. (2015). For this reason, ground-based measurements adopted the correction factors to cross section database. However the bias effect for the cross section difference is limited as shown in Figure 2, and the correction factor for the cross section database in the previous studies cannot be adopted to the space-borne measurements. From Kleipool et al. (2008), the minimum LER is defined to be the 1% cumulative probability threshold, and frequent LER value is typically higher than minimum LER over clear ocean, although cloud screening was perfectly executed before LER calculation. To account for the difference between simulated and observed SCD, the LUT was re-calculated by changing condition to the surface albedo of 0.10. The corrected result is shown in Figure 3(b), where the R^2 is 0.865 similar to that before the correction, but the negative bias is removed to 0.98±0.05 and the regression line slope is 1.123. Although the

comparison result is not perfect, the calculation by the VLIDORT simulates the satellite observation and can be used for sensitivity tests to retrieve aerosol height.

3. Sensitivity test

3.1. Sensitivity of the O4Is to the AEH

The sensitivity of the O4I to the AEH is investigated for its absorption bands at 340, 360, 380, and 477 nm. Figure 4 shows the O4I as a function of the AEH and the three different aerosol types of MITR, WASO and COPO at 360, 380, and 477 nm, respectively. The vertical error bar represents the fitting error estimated by the residual spectra from the DOAS fitting (e.g., Stutz and Platt, 1996). For the calculation shown in the figures, the following geometries are assumed: a solar zenith angle (SZA) of 30 degrees, a viewing zenith angle (VZA) of 30 degrees, and a relative azimuth angle (RAA) of 100 degrees. Note that insignificant SCD value was estimated at 340 nm due to the large spectra fitting error. In these three figures, the O4Is show the AEHs ranging from 1.0 to 5.0 km, and for the AODs of 1.0 and 2.5 at 500 nm, which could be due to the existence of thick aerosol layers. For the sensitivity result, the decrease rate of the O4I value in the 1 km interval of AEH ($-dO_4/dZ$) is defined as equivalent O4I difference converting from O4I difference between neighbor AEH in same AOD condition.

The O4Is are estimated at 360 and 380 nm band as shown in Figure 4(a) ~ (f). The O4I is significantly decreased with increasing AEH at 360 and 380 nm for all aerosol types. However negative O4Is are occasionally estimated at 360 nm. Furthermore the fitting errors are too large to estimate the AEH, which range from 160 to 410 at 360 nm and from 350 to 1060 at 380 nm. From large fitting error with small

306 O4I, the fitting results are insignificant at these two absorption bands.

307 On the other hand, the sensitivity of the O4I at 477 nm has significance to
308 estimate AEH. The mean value of $-dO_4/dZ$ is estimated to be 87, 290, and 190 for the
309 MITR, WASO, and COPO when the AOD is 1.0, respectively. The mean value of -
310 dO_4/dZ on the AOD of 2.5 is estimated to be 94, 362, and 213 for the MITR, WASO,
311 and COPO, respectively. The calculated $-dO_4/dZ$ are significantly larger than the mean
312 O4I fitting errors of 58, which implies that the O4I at 477 nm is useful in estimating
313 the AEH. The small fitting errors at 477 nm are due to the larger O_4 absorption and
314 less interferences by other trace gases in this spectral window.

315 Figure 5 shows $-dO_4/dZ$ as changing viewing geometries. As enlarging
316 geometrical path length for viewing geometry, $-dO_4/dZ$ also increases because the path
317 length through the aerosol layer is also enlarged. The mean value of $-dO_4/dZ$ including
318 all cases of AEH is estimated to be 90 to 326 at SZA of 30.0 degree and VZA of 30.0
319 degree, while it is estimated to be 265 to 485 at SZA of 60.0 degree and VZA of 60.0
320 degree. Although aerosol scattering angle is changed by differ to SZA and VZA, the
321 O4I sensitivity to AEH is generally enlarging to increasing optical path length to the
322 viewing geometries. From this result, the accuracy for the AEH retrieval is potentially
323 better for large zenith angle cases than for low zenith angle cases.

324

325 **3.2. Error analysis**

326 Errors are also estimated in terms of key variables in the estimation of the O4I at
327 477 nm, with the variables and their dimensions as summarized in Table 3. For the
328 error analysis of AEH retrieval, characteristics for all of extinction material are
329 essential to consider. In this study, errors are analyzed in terms of AOD, aerosol

vertical distribution, particle size and SSA for aerosol amount and properties. Surface albedo variation is also considered to represent surface condition. To estimate the error amount, the AEH error is converted from the half of O4I difference between adding and deducting perturbation of variables as shown in equation (1).

$$\varepsilon(Z) = \left| \frac{O4I(x+\delta x,Z) - O4I(x-\delta x,Z)}{2.0 \times dO4I/dZ(x,Z)} \right| \quad (1)$$

where $\varepsilon(Z)$ is the AEH error amount due to variable of error source, x, in AEH of Z, and δx is perturbation of AEH retrieval error source. The $\varepsilon(Z)$ value also depends on viewing geometries. Therefore $\varepsilon(Z)$ is represented for specific geometries together with averaging over all geometries.

3.2.1. AOD

The O4I at 477 nm has sensitivity not only for AEH but for AOD as shown in Figure 4(g) ~ (i). Because the radiance extinction by aerosol changes depending on AOD, the optical path length of TOA radiance is also affected by AOD. For different AODs (τ_a), the O4I at AEHs of 1.0 and 3.0 km is shown in Figure 6 for the same geometry assumed in Figure 4. From OMI standard products, the expected error of the AOD is 0.1 or 30% which ever is larger, and 0.1 or 20% which ever is larger for the absorbing and the non-absorbing aerosol over ocean, respectively. In this study the uncertainty of AOD is assumed to be 0.1, although uncertainty of AOD would be larger than the assumed value in large AOD. The decreasing rate of the O4I ($-dO_4/d\tau_a$), which defines O4I reduction with AOD increase by 0.1, is found to be larger for the AEH at 3.0 km than for that at 1.0 km. Among the three aerosol types, the $-dO_4/d\tau_a$ is found to be the least for the WASO, which has stronger scattering characteristics than

353 other two aerosol types. In addition, the sensitivity for WASO showed negative -
354 $dO_4/d\tau_a$ for small AOD at low AEH, which has small shielding effect, due to the large
355 SSA of WASO. The mean $-dO_4/d\tau_a$ values are estimated to be 1.2%, 0.9%, and -0.1%
356 for the AEH of 1.0 km as the AOD changes by 0.1 for the MITR, COPO, and WASO,
357 respectively, whereas they are estimated to be 2.3%, 2.1%, and 1.0% for the AEH of
358 3.0 km with respect to the same AOD changes for the three different type, respectively.
359 Figure 7 shows the expected error in AEH due to retrieval uncertainty of AOD
360 from observation. Because O_4 concentration exponentially decreases as the altitude
361 increases, the sensitivity to AEH becomes weak at high AEHs. In addition, aerosol
362 signal is relatively weak for low AOD. From these reasons, the AEH retrieval error
363 due to AOD uncertainty is maximized for the high AEH with low AOD cases for all
364 aerosol types. The maximum retrieval error is 2.0, 0.7, and 4.4 km for COPO, WASO,
365 and MITR for the case at AEH of 4.0 km and AOD of 0.4, which is least sensitive case
366 for AEH. For AOD of 0.4, however, the retrieval error due to AOD uncertainty is 0.3,
367 0.2, and 0.4 km for COPO, WASO, and MITR for the case at AEH of 1.0 km. Except
368 for AEH lower than 4 km and AOD larger than 0.4, the retrieval error of AEH is less
369 than 1.0 km for all viewing geometries and all aerosol types.
370 Furthermore, the AEH error for AOD uncertainty is also dependent on viewing
371 geometries. Overall, the AEH error becomes larger for short light paths and smaller
372 for long light paths. Figure 8 shows the viewing geometry dependence of AEH error
373 for AOD of 1.0. With the increase in effective optical path length, the radiance signal
374 from aerosol is also enhanced. In general, the AEH error decreases with increasing
375 viewing geometries. For WASO case, however, the AEH error is smaller for short path
376 length than long path length in low AEH case. For thin aerosol layer situation, the

377 radiance is enhanced by scattering aerosol which results in increasing optical path
378 length. In the small SZA and VZA, it effectively brings albedo effect dominant for
379 aerosol layer. With increasing SZA and VZA, however, the shielding effect due to
380 aerosol layer enhances because radiance has to pass through long path through aerosol
381 layer. For this reason, the smallest error case is inflection point of AOD sensitivity,
382 which is corresponds to turnaround point between with larger shielding effect than
383 albedo effect.
384
385 **3.2.2. SSA**
386 Torres *et al.* (1998) showed that the result of the SSA from OMI can be
387 overestimated due to the cloud contamination, although aerosol retrieval algorithm
388 considers existence of cloud in sub-pixel. Furthermore, the SSA varies widely for
389 different aerosol types. Therefore, the sensitivity of O4I to the SSA variation is
390 estimated for the same geometries used in the previous tests. To estimate O4I
391 sensitivity to the SSA variation, imaginary part of refractive index value corresponding
392 to 10% variability for SSA is changed after fixing real part of refractive index. The
393 mean O4I changes by 106, 282, and 205 for MITR, WASO, and COPO, respectively,
394 with respect to 10% of its SSA deviation. To compare the difference for WASO and
395 COPO, it is proportional to the absolute values of the SSA for all simulated cases. In
396 addition, the difference for MITR is smaller than those for COPO, because less
397 fraction of back scattering in coarse mode particle makes less sensitivity of O4I.
398 Figure 9 shows the AEH error due to SSA variation by 10%. Because of AEH
399 sensitivity characteristics as shown in section 3.1, which explained its low sensitivity,
400 thus large error for high AEH and low AOD cases. However, the AEH errors are less

than 1 km for COPO aerosol type. For AOD of 1.0, the AEH error due to SSA variation is estimated to be 610 to 900 m for the COPO type. Furthermore, the error is calculated to range from 270 to 1220 m and from 930 to 1400 m for COPO and WASO type, respectively, if AEH is 3 km, frequently assumed reference altitude in aerosol retrieval algorithm (e.g., Torres et al., 1998). For MITR, dust-like type aerosol, AEH error, which ranges from 410 to 1430 m for AOD of 1.0, is generally the largest compared to those of other aerosol types. In general, uncertainty of aerosol optical properties is large for thin aerosol layer case, thus the AEH as well.

3.2.3. Particle size

Aerosol particle size have noticeable effects phase function, thus the directional scattered intensity. However, most of aerosol retrieval algorithm assumes aerosol particle size depending on its type as an input parameter to RTM calculation. Although aerosol type is categorized, however, physical properties of aerosol can be changed according to the source type and transport characteristics. In the OMI aerosol algorithm, size distribution is one of error sources for the AOD.

Figure 10 shows the AEH error due to particle size change. For error estimation, mode radius difference for number size distribution is assumed to be ±20%, which set to be 4 times larger than those from the error budget study for OMI standard product (Torres et al., 2002). Overall, O4I difference is within the order of 100. The coarse mode aerosol, MITR in this study, results in the largest O4I difference for all cases, thus the largest AEH error for MITR which is estimated to range from 0.2 to 2.7 km. On the other hand, the error ranges from 0.03 to 0.5 km and from 0.2 to 1.9 km for WASO and COPO, respectively. The largest AEH errors for three aerosol types are

425 estimated for the case with AOD of 0.4 and AEH at 5.0 km.

426

427 **3.2.4. Surface Albedo**

428 As the surface albedo affects the $-dO_4/dZ$, the sensitivity of the O4I is also tested
429 with respect to the surface albedo difference of 0.02. The difference of climatological
430 surface albedo between that obtained from the total ozone monitoring spectrometer
431 (TOMS) and the global ozone monitoring experiment (GOME) was known to be up to
432 0.02 (Koelemeijer *et al.*, 2003). Table 4 shows the sensitivity of the O4I with respect to
433 the change in the surface albedo. The absolute difference of O4I due to surface albedo
434 variation is below 85. Because aerosol layer shut off the reflected radiance from
435 surface, the absolute difference of O4I value decreases as aerosol amount increase.
436 Furthermore, it is found that the difference of O4I due to surface albedo change is
437 higher for the absorbing aerosol than the non-absorbing aerosol, which can be
438 explained by the albedo effect to the O4I is larger for the absorbing aerosol. In terms of
439 AEH change, the O4I difference increases as AEH increase. For low AEH case, optical
440 path length of reflected radiance from surface to aerosol layer is relatively short as
441 compared to high AEH case. For this reason, the O4I sensitivity for surface albedo is
442 reduced by high concentration of aerosol near the surface for the low AEH case.

443 Figure 11 shows the expected retrieval error of AEH due to surface albedo
444 difference as changing AEH with respect to AOD and types. As mentioned in previous
445 section, the $-dO_4/dZ$ is small in high AEH and low AOD cases. Furthermore, the
446 albedo sensitivity increases as AEH increase and AOD decrease. As a result, the AEH
447 error is frequently larger than 1 km for high AEH with small AOD, especially AOD
448 less than 0.4. Because reflected radiance from surface is dominant for thin aerosol case,

449 the AEH error in high AEH with low AOD shows the largest value as compared to
450 previous error analysis. However, the AEH error sharply decreases as AOD increases
451 and AEH decreases, which is aerosol signal dominant case, because characteristics of
452 aerosol is the same as the reference case. Especially for MITR, 4 simulation cases,
453 AOD = 0.4 with AEH > 3.0 km and AOD = 1.0 with AEH = 5.0 km, show the AEH
454 error larger than 1 km. Because $-dO_4/dZ$ is too small in these cases, AEH retrievals in
455 four simulation cases show limitation as a reliable result. For COPO and WASO,
456 however, all the case in AEH < 3.0 km, which directly influence surface concentration,
457 show error less than 750 m even for the assumed AOD of 0.4. In addition, errors less
458 than 500 m are found for AOD > 1.0 with AEH < 3.0 km.
459
460 **3.2.5. Vertical distribution**
461 Aerosol vertical distribution is largely varied by distance from source, and
462 atmospheric dynamics during aerosol transport, and sink mechanism in reality. To
463 estimate the AEH error due to variation of aerosol vertical distribution, the half-width
464 of GDF distribution was doubled for comparison. Although this study is not able to
465 show all kinds of aerosol vertical distributions due to its large variability in profile,
466 aerosol vertical distribution by changing the half-width of GDF distribution can reflect
467 large-scale changes in its vertical profile.
468 Table 5 shows the mean AEH errors between the two vertical profiles of aerosol
469 as AOD changes. As the aerosol vertical profile is changed with increasing its widths,
470 the difference of O4I ranges from 100 to 430. Because aerosol vertical profile
471 simultaneously affects aerosol concentration and layer thickness, the O4I difference
472 shows large value as the vertical distribution changes. For this reason, the AEH error is

larger than 2.5 km for all aerosol types and AEH simulation with AOD of 0.4. The estimated errors caused solely by the change between the two aerosol vertical profiles, range 1477±602, 722±190, and 671±265 m for the MITR, COPO, and WASO, respectively, for AOD greater than 1.0.

3.3. Error budget

Table 6 shows the summary of the total error budget for the AEH estimation with a list of the major error sources and their values, assuming errors in each variable in OMI standard products. To convert the O4I difference to the AEH error, the difference of O4I due to the respective error source is divided by that from the change of the AEH in each bin of the AOD and AEH as shown in section 3.2, with the simulation cases over 58,800 runs listed in Table 3 used to calculate mean and standard deviation of errors. Because of weak signal sensitivity to AEH sensitivity for AOD of 0.4 and AEH at 5.0 km as shown in previous section, this simulation case is omitted in calculating statistical values for error budget. In summary, the total number of aerosol simulations for the combination of AOD and AEH includes 39 cases.

The mean errors from 10% variation in the SSA for all of the variable conditions in Table 3 correspond to 726, 576, and 1047 m for the MITR, COPO, and WASO, respectively. For the total error budget calculations, however, 5% change in the SSA was used according to Torres *et al.* (2007), which reported the variation of the SSA less than 0.03 for the given aerosol type. The error from the vertical distribution is estimated to be 720, 1480, and 690 m for the COPO, MITR and WASO, respectively.

The errors from the SSA and the aerosol profile shape are the two important error sources in estimating the AEH, followed by the errors related to the AOD and the

surface albedo. From these results, the errors of the AEH due to the error from OMI AOD of 0.1 and the surface albedo of 0.02 are less than 300 m for WASO and COPO, and about 400 m for MITR. However, the AEH error from surface albedo is important for cases with low AOD at high AEH, which is surface reflectance dominant case.

The mean errors from 20% variation in the aerosol particle size are 726, 576, and 1047 m for the MITR, COPO, and WASO, respectively. Torres et al. (2002) assumed the variation of size distribution to be 5%. For the total error budget calculations assumed by 5% change in the particle size, the AEH errors are less than 100 m. In addition, the errors in the O4I, and thereby the AEH, are associated with the variations in the column amounts and the differences in the absorption cross section of each fitted trace gas for the spectral analysis. The variations in the column amounts of trace gases and the differences in the absorption cross section values do not affect significantly in calculating the O4I. However, the O_4 vertical column density is changed by the change in atmospheric pressure. In East Asia, the surface pressure over ocean is 1010.9±29.6 (3-sigma) hPa from NCEP Reanalysis 2 data since 2004. In clear case, the difference of O4I due to the ±3% for pressure variation is 3.4±0.1% in all geometries.

Furthermore, the AEH error in terms of inaccurate spectral wavelength calibration is estimated based on the assumed errors of ±0.02 nm, which corresponds to 0.1 pixels for OMI. Although it is well known that the accuracy in the spectral wavelength calibration before the DOAS fitting affects the trace gas SCD retrieval, the errors in the O4I associated with the wavelength shift of the sub-pixel scale are estimated to be negligible due to the broad O_4 absorption band width around 477 nm.

Finally, the total error budget in the AEH retrieval is estimated based on the error analysis with respect to error sources. Note that the result of error analysis for SSA

explains a half and a quarter for size parameter in calculating the total error budget. Overall, the total error budget in the AEH retrieval is estimated to be 739, 1276, and 846 m for the COPO, MITR, and WASO, respectively, with the exception of the contribution of the errors in the aerosol vertical profiles. Therefore accurate assumption for optical properties of aerosol is essential to develop the retrieval algorithm of aerosol height.

4. Case study

To demonstrate the feasibility from real measurements, the AEHs are derived using hyperspectral data from OMI. OMI channels are composed of UV-1 (270-314 nm), UV-2 (306-380 nm), and a visible wavelength range (365-500 nm) with a spectral resolution (FWHM) of 0.63, 0.42, and 0.63 nm, respectively (Levelt *et al.*, 2006). The spatial resolution is 13 km × 24 km at nadir in "Global Mode". In the present study, the spectral data over the visible wavelength range are used to derive the O4I at 477 nm and the AEH information.

Figure 12 describes an AEH retrieval algorithm for the case study. In retrieving AEH, AOD is obtained from MODIS standard product (e.g., Levy et al., 2007). Although OMI aerosol product provides AOD at 500 nm, AOD from OMI was partially affected by aerosol height and suffered from cloud contamination due to its large footprint (Torres et al., 2002). For this reason, AOD from MODIS allocated to the OMI pixels as a reference AOD for the AEH retrieval. For type selection, the AE from MODIS and AI from OMI is respectively used for the information of size and absorptivity, to classify aerosol type into four following the method from Kim et al. (2007) and Lee et al. (2007). After determining AOD and aerosol type, LUT, which is

generated as functions of geometries (SZA, VZA, and RAA), aerosol types and AODs, is used to determine the AEH information by using comparison between simulated and measured O4I value. The variables and their dimensions for the LUT calculations are shown in Table 7. Due to the limitation of the accuracy of aerosol type classification and those of AOD over land, this study estimates the AEH only over ocean surface. Although temporal and spatial variation of surface albedo influences the AEH result from error study, surface albedo is assumed to be a fixed value of 0.10, which is used in sensitivity study. For case study, the LUT of O4I is developed by the aerosol model based on AERONET data over East Asia. Extensive AERONET dataset over East Asia are used to provide represent aerosol optical properties for the LUT calculation.

Figure 13 shows the results of the retrieved AEH during the Asian dust event on March, 31, 2007. MODIS products of AOD and FMF on this date show that thick dust layer with the AOD up to 1.0 from China to the Yellow sea [Figure 13(b)] and the FMF ranging from 0.2 to 0.4, indicating the dominance of coarse-mode particles [Figure 13(c)]. Using the basis of the current algorithm with the pre-determined AOD and type, the mean retrieved AEH is 2.3±1.3 km over 647 pixels in East Asia [Figure 13(d)]. The retrieved result is compared with the backscattering intensity from the CALIOP observation over Yellow sea as shown in Figure 13(e). From CALIOP observation, the aerosol layer height over Yellow sea is located around 1 km altitude for most observed regions. Over the Yellow sea domain in 35~40 ˚N and 120~130 ˚E, the AEH from OMI is 1.5±1.1 km over 166 pixels, which is within 1 km difference from CALIOP. From the retrieved result, the retrieved AEH is successfully retrieved within expected error, and the investigated algorithm quantitatively estimates the AEH over East Asia.

569 Figure 14 is another case study of the retrieved AEH on February, 21, 2008.
570 MODIS products of AOD and FMF on this date show thick anthropogenic aerosol
571 transported with the AOD ranging from 0.6 to 1.0 [Figure 14(b)] and the FMF ranging
572 from 0.8 to 1.0 [Figure 14(c)] all over Yellow sea. The mean retrieved AEH is 1.4±1.2
573 km over 1480 pixels in East Asia as shown in Figure 14(d). On this date, CALIOP
574 passed over coastal line between China and Yellow Sea. The aerosol layer height
575 ranged from 0.5 to 2.5 km during the overpass over East Asia as shown in Figure 14(e).
576 The AEH from OMI is 0.6±0.4 km over 601 pixels in 30~40 ˚N and 120~125 ˚E.
577 Contrary to large spatial variation of the AEH from CALIOP, the AEH from OMI
578 shows spatially stable values on this date.
579 Figure 15 shows the scatter plot of AEH between CALIOP and OMI on the date
580 listed in Table 8, which lists aerosol transport cases over East Asia with simultaneous
581 observations by OMI and CALIOP in 2007 and 2008. Because the O4I sensitivity for
582 AEH is not large at AEH higher than 4 km, the comparison test was limited to cases
583 with AEH less than 4.5 km from OMI. For data collocation, the latitude and longitude
584 difference between two sensors are within 0.25 degree. Figure 15(a) shows the
585 comparison of AEH from OMI and CALIOP with MODIS AOD larger than 0.5. It is
586 assumed that the reference expected error (EE) is 1 km (Fishman et al., 2012). Almost
587 60% of retrieved pixel shows the AEH result within the EE. Because of large AEH
588 error for low AOD, the accuracy of AEH result from OMI is poor. Furthermore, this
589 case study assumes constant surface albedo value over ocean. However, ocean surface
590 albedo is also changed by turbidity due to sediments and wind. For this reason, the
591 AEH error is enlarged for low AOD cases. If threshold of AOD for the comparison is
592 set to be 1.0, the proportion of pixel within EE improves up to 80% as shown in Figure

593 15(b). Furthermore, the correlation of the AEH between the two sensors is 0.62 as a
594 slope with 0.65 of correlation coefficient (R) on thick aerosol layer cases. Therefore,
595 the AEH algorithm from OMI provides the reasonable information about the parameter
596 of aerosol vertical distribution, if accurate aerosol model is provided for forward
597 calculation.
598
599 **5. Summary & discussion**
600 The sensitivities of the O4I at 340, 360, 380, and 477 nm bands are investigated
601 with RTM calculations to derive the AEH using the space-borne hyperspectral data.
602 Among these O_4 absorption bands, the O4I at 477 nm is considered to be suitable for
603 the AEH retrieval. In addition to the AEH, AOD, aerosol type, aerosol vertical profile,
604 particle size, and surface albedo are also found to have effects on the O4I at 477 nm,
605 while the spectral calibration and cross section of the atmospheric gases have
606 negligible effects on the O4I. The major error source for the AEH retrieval is the
607 uncertainty in SSA, which leads to the AEH error ranging from 270 to 1400 m with the
608 SSA perturbation by 10%. In addition, the profile shape is also a major error source for
609 the AEH estimation. According to the error estimations, the total errors are 739, 1276
610 m, and 846 m for absorbing, dust, and non-absorbing aerosol, respectively, due to
611 combined uncertainties of the variation from AOD, SSA, particle size, and surface
612 albedo.
613 In addition to the sensitivity analysis, an algorithm for the AEH derivation is
614 developed for the first time based on a LUT that consists of the O4I in terms of the
615 AEH, AOD, aerosol types, surface albedo, and measurement geometries. After the
616 determination of AOD and aerosol types from the MODIS, the AEH value is derived

over East Asia by the current algorithm using OMI measurement data. To consider the accuracy of AOD and aerosol types, the result is shown over ocean surface. From several cases for the long-range transport of aerosol over East Asia, the derived AEH shows reasonable value as compared to aerosol layer height from CALIOP with the correlation coefficient of 0.62 for AOD larger than 1.0. In addition, 80% of estimated AEH from OMI showed error less than 1 km in AEH.

There are many works to be done to improve the newly introduced algorithm as it requires the products from MODIS to determine the AOD and aerosol types prior to the AEH retrieval. The vertical distribution and the optical properties of the aerosol need to be quantified using the combination of observation database, such as MPLNET and AERONET. Furthermore, the spatial variation of the AOD, surface pressure and the contamination by the cloud in the sub-pixel scale need to be investigated as they are also thought to affect the retrieved results. If the surface reflectance can be characterized with sufficient accuracy, the retrieval of the AEH can be extended to over land. In addition, the O4I method in this study can be applied to the surface pressure estimation in clear regions.

Acknowledgements

This work was supported by the Eco Innovation Program of KEITI (ARQ201204015), Korea, and it was also supported by the Brain Korea plus program.

References

Accarreta, J. R., De Haan, J. F., and Stammes, P.: Cloud pressure retrieval using the O2-O2 absorption band at 477 nm, *J. Geophys. Res.*, *109*, D05204, doi:10.1029/2003JD003915, 2004

Ahn, C., Torres, O., and Jethva, H.: Assessment of OMI near-UV aerosol optical depth over land, *J. Geophys. Res., 119,* 2457-2473, doi:10.1002/2013JD020188, 2014.

Albrecht, B. A.: Aerosols, cloud microphysics, and fractional cloudiness, *Science, 245*, 1227-1230, 1989.

Bogumil, K., Orphal, J., Burrows, J. P., and Flaud, J. M.: Vibrational progressions in the visible and near-ultraviolet absorption spectrum of ozone, *Chem. Phys. Lett.*, *349*, 241-248, 2001.

Castellanos, P., Boersma, K. F., Torres, O., and De haan, J. F.: OMI tropospheric NO2 air mass factors over South America: effects of biomass burning aerosols, *Atmos. Meas. Tech. Discuss, 8*, 2683-2733, 2015.

Chiang, C. -W, Chen, W. -N., Liang, W. -A., Das, S. K., and Nee, J.-B.: Optical properties of tropospheric aerosols based on measurements of lidar, sun-photometer and visibility at Chung-Li (25˚N, 121˚E), *Atmos. Env., 41*, 4128-4137, 2007.

Chimot, J., Vlemmix, T., Veefkind, J. P., De Haan, J. F., and Levelt, P. F.: Impact of aerosols on the OMI tropospheric NO2 retrievals over industrialized regions: how accurate is the aerosol correction of cloud-free scenes via a simple cloud model?, *Atmos. Meas. Tech. Discuss, 8*, 8385-8437, 2015.

Chou, M. -D, Chan, P. -K., and Wang, M.: Aerosol radiative forcing derived from SeaWiFS-Retrieved aerosol optical properties, *J. Atmos. Sci., 59*, 748-757, 2002.

Christopher, S. A., Zhang, J., Kaufman, Y. J., and Remer, L. A.: Satellite-based assessment of top of atmosphere anthropogenic aerosol radiative forcing over

664 cloud-free oceans, *Geophys. Res. Lett*, *33*, L15816, doi:10.1029/2005GL025535,
665 2006.
666 Chu, D. A.: Analysis of the relationship between MODIS aerosol optical depth and
667 PM2.5 in the summertime US., *Optics & Photonics. International Society for*
668 *Optics and Photonics,* 2006.
669 Chung, E. C., Ramanathan, V., Kim, D., and Podgorny. I. A.: Global anthropogenic
670 aerosol direct forcing derived from satellite and ground-based observations, *J.*
671 *Geophys. Res., 110,* D24207, doi:10.1029/2005JD006356, 2005.
672 Clemer, K., Van Roozendael, M., Fayt, C., Hendrick, F., Hermans, C., Pinardi, G.,
673 Spurr, R., Wang, P., and De Maziere, M.: Multiple wavelength retrieval of
674 tropospheric aerosol opticalproperties from MAXDOAS measurements in Beijing,
675 *Atmos. Meas. Tech., 3*, 863-878, doi:10.5194/amt-3-863-2010, 2010.
676 Curier, R. L., Veefkind, J. P., Braak, R., Veihelmann, B., Torres, O., and de Leeuw, G.:
677 Retrieval of aerosol optical properties from OMI radiances using a
678 multiwavelength algorithm: Application to western Europe, *J. Geophys. Res., 113*,
679 D17S90, doi:10.1029/2007JD008738, 2008.
680 Dirksen, R. J., Boersma, K. F., de Laat, J., Stammes, P., van der Werf, G. R., Martin, M.
681 V., and Kelder, H. M., An aerosol boomerang: Rapid around-the-world transport of
682 smoke from the December 2006 Australian forest fires observed from space, *J.*
683 *Geophys. Res., 114*, D21201, doi:10.1029/2009JD012360, 2009.
684 Dubovik, O., Holben, B., Eck, T. F., Smirnov, A., Kaufman, Y. J., King, M. D., Tanre,
685 D., and Slutsker, I.: Variability of absorption and optical properties of key aerosol
686 types observed in worldwide locations, *J. Atmos. Sci., 59*, 590-608, 2002.
687 Dubuisson, P., Frouin, R., Dessaily, D., Duforet, L., Leon, J. –F., Voss, K., and Antoine,
688 D.: Estimating the altitude of aerosol plumes over the ocean from reflectance ratio
689 measurements in the O2 A-band, *Remote Sens. Environ.*, *113*, 1899-1911,
690 doi:10.1016/j.rse.2009.04.018, 2009.
691 Fish, D. J., and Jones, R. L.: Rotational Raman scattering and the ring effect in zenith-
692 sky spectra, *Geophys. Res. Lett., 22*, 811-814, 1995.
693 Fishman, J., Iraci, L. T., Al-Saadi, J., Chance, K., Chavez, F., Chin, M., Coble, P.,
694 Davis, C., DiGiacomo, P. M., Edwards, D., Eldering, A., Goes, J., Herman, J., Hu,
695 C., Jacob, D. J., Jordan, C., Kawa, S. R., Key, R., Liu, X., Lohrenz, S., Mannino,

696 A., Natraj, V., Neil, D., Neu, J., Newchurch, M., Pickering, K., Salisbury, J., Sosik,
697 H., Subramaniam, A., Tzortziou, M., Wang, J., and Wang, M.: The United States'
698 Next Generation of Atmospheric Composition and Coastal Ecosystem
699 Measurements: NASA's Geostationary Coastal and Air Pollution Events (GEO-
700 CAPE) Mission. *Bull. Amer. Meteor. Soc., 93*, 1547-1566, 2012.
701 Friess, U., Monk, P. S., Remedios, J. J., Rozanov, A., Sinreich, R., Wagner, T., and
702 Platt, U.: MAX-DOAS O4 measurements: A new technique to derive information
703 on atmospheric aerosols: 2. Modeling studies, *J. Geophys. Res., 111*, D14203,
704 doi:10.1029/2005JD006618, 2006.
705 Hayasaka, T., Satake, S., Shimizu, A., Sugimoto, N., Matsui, I., Aoki, K., and Muraji,
706 Y.: Vertical distribution and optical properties of aerosols observed over Japan
707 during the Atmospheric Brown Clouds-East Asia Regional Experiment 2005, *J.*
708 *Geophys. Res., 112*, D22S35, doi:10.1029/2006JD008086, 2007.
709 Haywood, J. M. and Shine, K. P.: The effect of anthropogenic sulfate and soot aerosol
710 on the clear sky planetary radiation budget, *Geophys. Res. Lett., 22*, 603-606, 1995.
711 Herman, J. R., Bhartia, P. K., Torres, O., Hsu, C., Seftor, C., and Celarier, E.: Global
712 distribution of UV-absorbing aerosols from Nimbus-7/TOMS data, *J. Geophys.*
713 *Res., 102*(D14), 16911-16922, 1997.
714 Hermans, C., Vandaele, A. C., Carleer, M., Fally, S., Colin, R., Jenouvrier, A., Coquart,
715 B., and Merienne, M.: Absorption Cross-sections of atmospheric constituents: NO2,
716 O2, and H2O, *Environ. Sci. Poll. Res., 6(3)*, 151-158, 1999.
717 Hermans, C., Vandaele, A. C., Fally, S., Carleer, M., Colin, R., Coquart, B., Jenouvrier,
718 A., and Merienne, M. F.: Absorption cross-section of the collision-induced bands
719 of oxygen from the UV to the NIR. In Weakly interacting molecular pairs:
720 unconventional absorbers of radiation in the atmosphere, (pp. 193-202), Springer
721 Netherlands, 2003.
722 Hess, M., Koepke, P., and Schult, I.: Optical properties of aerosols and clouds: The
723 software package OPAC, *B. Am. Meteorol. Soc., 79*(5), 831-844, 1998.
724 Higurashi, A., and Nakajima, T.: Detection of aerosol types over the East China Sea
725 near Japan from four-channel satellite data, *Geophys. Res. Lett, 29*(17), 1836,
726 doi:10.1029/2002GL015357, 2002.

727 Holzer-Popp, T., and Schroedter-Homscheidt, M.: Synergetic aerosol retrieval from
728 ENVISAT.In Proc. ERS/ENVISAT Symposium, Salzburg (Vol. 6, No. 10.9), 2004.
729 Hutchison, K. D., Smith, S., and Faruqui, S. J.: Correlating MODIS aerosol optical
730 thickness data with ground-based PM2.5 observations across Texas for use in a
731 real-time air quality prediction system, *Atmos. Env., 39*, 7190-7203, 2005.
732 Irie, H., Kanaya, Y., Akimoto, H., Iwabuchi, H., Shimizu, A., and Aoki, K.: Dual-
733 wavelength aerosol vertical profile measurements by MAX-DOAS at Tsukuba,
734 Japan, *Atmos. Chem. Phys., 9*, 2741-2749, 2009.
735 Irie, H., Takashima, H., Kanaya, Y., Boersma, K. F., Gast, L., Wittrock, F., Brunner, D.,
736 Zhou, Y., and Van Roozendael, M.: Eight-component retrievals from ground-based
737 MAX-DOAS observations, *Atmos. Meas. Tech., 4*, 1027-1044, 2011.
738 Irie, H., Nakayama, T., Shimizu, A., Yamazaki, A., Nagai, T., Uchiyama, A., Zaizen, Y.,
739 Kagamitani, S., and Matsumi, Y.: Evaluation of MAX-DOAS aerosol retrievals by
740 coincident observations using CRDS, lidar, and sky radiometer in Tsukuba, Japan,
741 *Atmos. Meas. Tech., 8*, 2775-2788, 2015.
742 Jeong, M., -J., and Hsu, N. C.: Retrievals of aerosol single-scattering albedo and
743 effective aerosol layer height for biomass-burning smoke: Synergy derived from
744 "A-Train" sensors, *Geophys. Res. Lett.*, Vol. 35, L24801,
745 doi:10.1029/2008GL036279, 2008.
746 Jethva, H., Torres, O., and Ahn, C.: Global assessment of OMI aerosol single-scattering
747 albedo using ground-based AERONET inversion, *J. Geophys. Res., 119*, 9020-
748 9040, doi:10.1002/2014JD021672, 2014.
749 Johnson, B. T., Heese, B., McFarlane, S. A., Chazette, P., Jones, A., and Bellouin, N.:
750 Vertical distribution and radiative effects of mineral dust and biomass burning
751 aerosol over West Africa during DABEX, *J. Geophys. Res.*, 113, D00C12,
752 doi:10.1029/2008JD009848, 2008.
753 Jones, A., Roberts, D. L., and Slingo, A.: A climate model study of indirect radiative
754 forcing by anthropogenic sulphate aerosols, *Nature, 370*, 450-453, 1994.
755 Jones, T. A., and Christopher, S. A.: MODIS derived fine mode fraction characteristics
756 of marine, dust, and anthropogenic aerosols over the ocean, constrained by
757 GOCART, MOPITT, and TOMS, *J. Geophys. Res., 112*, D22204,
758 doi:10.1029/2007JD008974, 2007.

759 Kaufman, Y. J., Tanre, D., and Boucher, O.: A satellite view of aerosols in the climate
760 system, *Nature, 419,* 215-223, 2002.
761 Kim, J., Lee, J., Lee, H. C., Higurashi, A., Takemura, T., and Song, C. H.: Consistency
762 of the aerosol type classification from satellite remote sensing during the
763 Atmospheric Brown Cloud – East Asia Regional Experiment campaign, *J.*
764 *Geophys. Res., 112*, D22S33, doi:10.1029/2006JD008201, 2007.
765 Kleipool, Q. L., Dobber, M. R., de Haan, J. F., and Levelt, P. F.: Earth surface
766 reflectance climatology from 3 years of OMI data, *J. Geophys. Res.*, 113,
767 D18308, doi:10.1029/2008JD010290, 2008.
768 Koelemeijer, R. B. A., de Haan, J. F., and Stammes, P.: A database of spectral surface
769 reflectivity in the range 335-772 nm derived from 5.5 years of GOME
770 observations, *J. Geophys. Res.,108*(D2), 4070, doi:10.1029/2002JD002429,
771 2003.
772 Kokhanovsky, A. A., and Rozanov, V. V.: The determination of dust cloud altitudes
773 from a satellite using hyperspectral measurements in the gaseous absorption band,
774 *Int. J. Rem. Sens., 31*, Nos. 9-10, 2729-2744, 2010.
775 Koppers, G. A. A., and Murtagh, D. P.: Retrieval of height resolved aerosol optical
776 thickness in the atmospheric band (Chapter 5), in G. A. A. Koppers, Radiative
777 transfer in the absorption bands of oxygen: Studies of their significance in ozone
778 chemistry and potential for aerosol remote sensing, Stockholm Univ., Stockholm,
779 Sweden, 1997.
780 Labonne, M., Breon, F. -M., and Chevallier, F.: Injection height of biomass burning
781 aerosols as seen from a spacebornelidar, *Geophys. Res. Lett., 34,* L11806,
782 doi:10.1029/2007GL029311, 2007.
783 Lee, H., Irie, H., Kim, Y. J., Noh, Y., Lee, C., Kim, Y., and Chun, K. J.: Retrieval of
784 aerosol extinction in the lower troposphere based on UV MAX-DOAS
785 measurements, *Aerosol Sci. Technol., 43(5),* 502-509, 2009.
786 Lee, H., Irie, H., Gu, M., Kim, J., and Hwang, J.: Remote sensing of tropospheric
787 aerosol using UV MAX-DOAS during hazy conditions in winter: Utilization of O4
788 absorption bands at wavelength intervals of 338-368 and 367-393 nm, Atmos. Env.,
789 doi:10.1016/j.atmosenv.2011.07.019, 2011.

790 Lee, J., Kim, J., Lee, H. C., and Takemura, T.: Classification of aerosol type from
791 MODIS and OMI over East Asia, *Asia-Pacific J. Atmos. Sci., 43*, 4, 343-357, 2007.
792 Lee, J., Kim, J., Song, C. H., Ryu, J. -H., Ahn, Y. –H., and Song, C. K.: Algorithm for
793 retrieval of aerosol optical properties over the ocean from the Geostationary Ocean
794 Color Imager, *Remote Sens. Environ., 114*, 1077-1088, 2010.
795 Levelt, P. F., van den Oord, G. H. J., Dobber, M. R., Maelkki, A., Visser, H., de Vries,
796 J., Stammes, P., Lundell, J. O. V., and Saari, H.: The Ozone Monitoring Instrument,
797 *IEEE T. Geosci. Remote., 44*(5), 1093-1101, 2006.
798 Levy, R. C., Remer, L. A., Mattoo, S., Vermote, E. F., and Kaufman, Y. J.: Second-
799 generation operational algorithm : Retrieval of aerosol properties over land from
800 inversion of Moderate Resolution Imaging Spectroradiometer spectral
801 reflectance, *J. Geophys. Res., 112*, D13211, doi:10.1029/2006JD007811, 2007.
802 Li, X., Brauers, T., Shao, M., Garland, R. M., Wagner, T., Deutschmann, T., and
803 Wahner, A.: MAX-DOAS measurements in southern China: Retrieval of aerosol
804 extinctions and validation using ground-based in-situ data, *Atmos. Chem. Phys.,*
805 *10*, 2079-2089, 2010.
806 Lin, J. -T., Martin, R. V., Boersma, K. F., Sneep, M., Stammes, P., Spurr, R., Wang, P.,
807 Van Roozendael, M., Clemer, K., and Irie, H.: Retrieving tropospheric nitrogen
808 dioxide from the Ozone Monitoring Instrument: effects of aerosols, surface
809 reflectance anisotropy, and vertical profile of nitrogen dioxide, *Atmos. Chem.*
810 *Phys., 14*, 1441-1461, 2014.
811 Lin, J. -T., Liu, M. -Y., Xin, J. -Y., Boersma, K. F., Spurr, R., Martin, R., and Zhang, Q.:
812 Influence of aerosols and surface reflectance on satellite NO_2 retrieval: seasonal
813 and spatial characteristics and implications for NOx emission constraints, *Atmos.*
814 *Chem. Phys. Discuss., 15*, 12653-12714, 2015.
815 Liu, Y., Sarnat, J. A., Kilaru, V., Jacob, D. J., and Koutrakis, P.: Estimating ground-
816 level PM2.5 in the Eastern United States using satellite remote sensing, *Environ.*
817 *Sci. Technol., 39*, 3269-3278, 2005.
818 Nakajima, T., and Higurashi, A.: A use of two-channel radiances for and aerosol
819 characterization from space, *Geophys. Res. Lett., 25(20)*, 3815-3818, 1998.

820 Newnham, D. A., and Ballard, J.: Visible absorption cross sections and integrated
821 absorption intensities of molecular oxygen (O_2 and O_4), *J. Geophys. Res., 103*, No.
822 D22, 28801-28816, 1998.
823 Omar, A. H., Winker, D. M., Kittaka, C., Vaughan, M. A., Liu, Z., Hu, Y., Trepte, C. R.,
824 Rogers, R. R., Ferrare, R. A., Lee, K. –P., Kuehn, R. E., and Hostetler, C. A.: The
825 CALIPSO automated aerosol classification and lidar ratio selection algorithm, *J.*
826 *Atmos. Oceanic Technol., Vol. 26*, 1994-2014, 2009.
827 Platt, U.: Differential optical absorption spectroscopy (DOAS), *Air monitoring by*
828 *spectroscopic technique*, 127, 27-84, 1994.
829 Platt, U., and Stutz, J.: *Differential absorption spectroscopy*, Springer Berlin Heidelberg,
830 2008.
831 Prospero, J. M.: Long-term measurements of the transport of African mineral dust to the
832 southeastern United States: Implications for regional air quality, *J. Geophys.*
833 *Res., 104(D13)*, 15917-15927, 1999.
834 Reid, J. S., Westphal, D. L., Livingston, J. M., Savoie, D. L., Maring, H. B., Jonsson, H.
835 H., Eleuterio, D. P., Kinney, J. E., Reid, E. A.: Dust vertical distribution in the
836 Caribbean during the Puerto Rico Dust Experiment, *Geophys. Res. Lett., 29*, 7,
837 1151, doi:10.1029/2001GL014092, 2002.
838 Remer, L. A., Kleidman, R. G., Levy, R. C., Kaufman, Y. J., Tanre, D., Mattoo, S.,
839 Martins, J. V., Ichoku, C., Koren, I., Yu, H., and Holben, B. N.: Global aerosol
840 climatology from the MODIS satellite sensors, *J. Geophys. Res., 113*, D14S07,
841 doi:10.1029/2007JD009661, 2008.
842 Sanders, A. F. J. and de Haan, J. F.: Retrieval of aerosol parameters from the oxygen A
843 band in the presence of chlorophyll fluorescence, *Atmos. Meas. Tech., 6*, 2725-
844 2740, 2013.
845 Sanghavi, S., Martonchik, J. V., Landgraf, J., and Platt, U.: Retrieval of optical depth
846 and vertical distribution of particulate scatterers in the atmosphere using O2 A-
847 and B-band SCIAMACHY observations over Kanpur: a case study, *Atmos.*
848 *Meas. Tech., 5*, 1099-1119, 2012.
849 Sasano, Y.: Tropospheric aerosol extinction coefficient profiles derived from scanning
850 lidar measurements over Tsukuba, Japan, from 1990 to 1993, *App. Opt., 35*(24),
851 4941-4952, 1996.

852 Seo, S., Kim, J., Lee, H., Jeong, U., Kim, W., Holben, B. N., Kim, S., Song, C. H., and
853 Lim, J. H.: Estimation of PM_{10} concentrations over Seoul using multiple
854 empirical models with AERONET and MODIS data collected during the
855 DRAGON-Asia campaign, *Atmos. Chem. Phys., 154*, 1-16, doi:10.5194/acp-15-
856 1-2015, 2015.
857 Shimizu, A., Sugimoto, N., Matsui, I., Arao, K., Uno, I., Murayama, T., Kagawa, N.,
858 Aoki, K., Uchiyama, A., and Yamazaki, A.: Continuous observation of Asian
859 dust and other aerosols by polarization lidars in China and Japan during ACE-
860 Asia, *J. Geophys. Res., 109*, D19S17, doi:10.1029/2002JD003253, 2004.
861 Sneep, M., De Haan, J. F., Stammes, P., Wang, P., Vanbauce, C., Joiner, J., Vasilkov, A.
862 P., and Levelt, P. F.: Three-way comparison between OMI and PARASOL
863 cloud pressure products, *J. Geophys. Res., 113*, D15S23,
864 doi:10.1029/2007JD008694, 2008.
865 Spurr, R. J. D., Kurosu, T. P., and Chance, K. V.: A linearized discrete ordinate
866 radiative transfer model for atmospheric remote-sensing retrieval, *J. Quant.*
867 *Spectro. Rad. Trans., 68*, 689-735, 2001.
868 Spurr, R. J. D.: Simultaneous derivation of intensities and weighting functions in a
869 general pseudo-spherical discrete ordinate radiative transfer treatment, *J. Quant.*
870 *Spectro. Rad. Trans., 75*, 129-175, 2002.
871 Spurr, R. J. D.: VLIDORT: A linearized pseudo-spherical vector discrete ordinate
872 radiative transfer code for forward model and retrieval studies in multilayer
873 multiple scattering media, *J. Quant. Spectro. Rad. Trans.*, *102*, 316-342, 2006.
874 Spurr, R., and Christi, M.: On the generation of atmospheric property Jacobians from
875 the (V)LIDORT linearized radiative transfer models, *J. Quant. Spectro. Rad.*
876 *Trans., 142*, 109-115, 2014.
877 Stutz, J., and Platt, U.: Numerical analysis and estimation of the statistical error of
878 differential optical absorption spectroscopy measurements with least-squares
879 methods, *Applied Optics, 35, 30*, 6041-6053, 1996.
880 Torres, O., Bhartia, P. K., Herman, J. R., Ahmad, Z., and Gleason, J.: Derivation of
881 aerosol properties from satellite measurements of backscattered ultraviolet
882 radiation: Theoretical basis, *J. Geophys. Res., 103*(14), 17099-17110, 1998.

Torres, O., Decae, R., Veefkind, P., and de Leeuw, G.: *OMI Aerosol Retrieval Algorithm*, OMI Algorithm Theoretical Basis Document, Vol. III, Clouds, Aerosols and Surface UV Irradiance, NASA-KNMI ATBD-OMI-03, pp. 47-71, 2002.

Torres, O., Bhartia, P. K., Sinyuk, A., Welton, E. J., and Holben, B. N.: Total Ozone Mapping Spectrometer measurements of aerosol absorption from space: Comparison to SAFARI 2000 ground-based observations, *J. Geophys. Res., 110,* D10S18, doi:10.1029/2004JD004611, 2005.

Torres, O., Tanskanen, A., Veihelmann, B., Ahn, C., Braak, R., Bhartia, P. K., Veefkind, P., and Levelt, P.: Aerosols and surface UV products from Ozone Monitoring Instrument observations: An overview, *J. Geophys. Res., 112*, D24S47, doi:10.1029/2007JD008809, 2007.

Twomey, S. A., Piepgrass, M., and Wolfe, T. L.: An assessment of the impact of pollution on the global albedo, *Tellus, 36B*, 356-366, 1984.

United States Committee on Extension to the Standard Atmosphere: *US Standard Atmosphere 1976, National Oceanic and Atmospheric Administration*, NASA., United States Air Force, Washington DC, USA, 1976.

Van Roozendael, M., and Fayt, C.: *WinDOAS 2.1 Software user manual*, Uccle, IASB/BIRA, 2001.

Vandaele, A. C., Hermans, C., Simon, P. C., Carleer, M., Colin, R., Fally, S., Merienne, M. F., Jenouvrier, A., and Coquart, B.: Measurements of the NO2 absorption cross-section from 42000 cm^{-1} to 10000 cm^{-1} (238-1000 nm) at 220 K and 294 K, *J. Quant. Spectrosc. Radiat. Transfer*, 59, 3-5, 171-184, 1998.

Veefkind, J. P., de Leeuw, G., Durkee, P. A., Russell, P. B., Hobbs, P. V., and Livingston, J. M.: Aerosol optical depth retrieval using ATSR-2 and AVHRR data during TARFOX, *J. Geophys. Res., 104(D2)*, 2253-2260, 1999.

Veihelmann, B., Levelt, P. F., Stammes, P., and Veefkind, J. P.: Simulation study of the aerosol information content in OMI spectral reflectance measurements, *Atmos. Chem. Phys.*, 7, 3115-3127, 2007.

Wagner, T., Dix, B., Friedeburg, C. V., Friess, U., Sanghavi, S., Sinreich, R., and Platt, U.: MAX-DOAS O_4 measurements: A new technique to derive information on

914 atmospheric aerosols- Principles and information content, *J. Geophys. Res., 109*,
915 D22205, doi:10.1029/2004JD004904, 2004.
916 Wagner, T., Beirle, S., Deutschmann, T., Grzegorski, M., and Platt, U.: Satellite
917 monitoring of different vegetation types by differential optical absorption
918 spectroscopy (DOAS) in the red spectral range*, Atmos. Chem. Phys., 7*, 69-79,
919 2007.
920 Wagner, T., Deutschmann, T., and Platt, U.: Determination of aerosol properties from
921 MAX-DOAS observations of the Ring effect, *Atmos. Meas. Tech., 2*, 495-512,
922 2009.
923 Wagner, T., Beirle, S., Deutschmann, T., and de Vries, M. P.: A sensitivity analysis of
924 Ring effect to aerosol properties and comparison to satellite observations, *Atmos.*
925 *Meas. Tech., 3*, 1723-1751, 2010.
926 Wang, J., and Christopher, S. A.: Intercomparison between satellite-derived aerosol
927 optical thickness and PM2.5 mass: Implications for air quality studies, *Geophys.*
928 *Res. Lett.,30*(21), 2095, doi:10.1029/2003GL018174, 2003.
929 Wang, P., Tuinder, O. N. E., Tilstra, L. G., and Stammes, P.: Interpretation of FRESCO
930 cloud retrievals in case of absorbing aerosol events, *Atmos. Chem. Phys., 12*,
931 9057-9077, 2012.
932 Watson, J. G., Chow, J. C., Lu, Z., Fujita, E. M., Lowenthal, D. H., Lawson, D. R., and
933 Ashbaugh, L. L.: Chemical mass balance source apportionment of PM10 during
934 the Southern California air quality study, *Aerosol Sci. Technol., 21(1)*, 1-36,
935 1994.
936 Yang, K., Liu, X., Bhartia, P. K., Krotkov, N. A., Carn, S. A., Hughes, E. J., Krueger, A.
937 J., Spurr, R. J. D., and Trahan, S. G.: Direct retrieval of sulfur dioxide amount
938 and altitude from spaceborne hyperspectral UV measurements: Theory and
939 application, *J. Geophys. Res., 115*, D00L09, doi:10.1029/2010JD013982, 2010.
940 Zhang, H., Lyapustin, A., Wang, Y., Kondragunta, S., Laszlo, L., Ciren, P., and Hoff, R.
941 M.: A multi-angle aerosol optical depth retrieval algorithm for geostationary
942 satellite data over the United States, *Atmos. Chem. Phys., 11*, 11977-11991,
943 2011.
944
945

946 **List of Tables**

955

List of Figures

985 **Tables**

986 Table 1. The database of cross section for DOAS fitting analysis.

Species	Temperature (K)	Reference
O_3	223, 243, and 273	Bogumil *et al.* (2001)
NO_2	220 and 294	Vandaele *et al.* (1998)
O_4	298	Hermans *et al.* (1999)

987

988 Table 2. Dimensions of LUT for the clear sky comparison.

Variable name	No. of Entries	Entries
SZA	7	0, 10, 20, 30, 40, 50, 60 degrees
VZA	7	0, 10, 20, 30, 40, 50, 60 degrees
RAA	10	0, 20, 40, 60, 80, 100, 120, 140, 160, 180 degrees

989 SZA : Solar zenith angle, VZA : Viewing zenith angle, RAA: Relative azimuth angle.

990

991 Table 3. Dimensions of simulation cases for the error analysis of the AEH retrieval.

Variable name	No. of Entries	Entries
SZA	7	0, 10, 20, 30, 40, 50, 60 degrees
VZA	7	0, 10, 20, 30, 40, 50, 60 degrees
RAA	10	0, 20, 40, 60, 80, 100, 120, 140, 160, 180 degrees
AOD	5	0.4, 1.0, 1.6, 2.5, 3.0
AEH	8	1.0, 1.2, 1.6, 2.0, 2.4, 3.0, 4.0, 5.0 km
Aerosol Model	3	MITR, WASO, COPO
Surface Albedo	1	0.10

992

993

994 Table 4. Absolute difference of O4I for changing surface albedo variation of 0.02.

	MITR	WASO	COPO
Maximum	81	85	76
Case [AOD,AEH]	[0.4,5.0]	[0.4,5.0]	[0.4,5.0]
Minimum	8	11	1
Case [AOD,AEH]	[3.0,1.0]	[3.0,1.0]	[3.0,1.0]
Mean	38±22	37±20	20±21

995

996

997 Table 5. The error for AEH due to the change of aerosol vertical distribution.

Reference shape (Exponential)	MITR (Gaussian)	WASO (Gaussian)	COPO (Gaussian)
Error for AEH [m]	1477±602	671±265	722±190

998

999

1000

1001 Table 6. Summary of error sources and total error budget for the AEH retrieval.

Error source	MITR	WASO	COPO
AOD (ΔAOD = 0.2)	387±740 m	105±131 m	218±358 m
SSA (10% change)	726±537 m	1047±194 m*	576±332 m
Surface Albedo ($\Delta\alpha$ = 0.02)	438±762 m	199±241 m	154±274 m
Particle Size (20% change)	352±174 m	72±56 m	315±213 m
Atmospheric Gases		< 5 m	
Atmospheric Pressure** (ΔP = 3%)		3.4±0.1% (O_4 SCD)	
Instrument (Shift : 0.02 nm)		<10 m	
Total Error	1276 m	846 m	739 m

1002 * Calculation results for the SSA decrease of 10%.

1003 ** For clear sky calculation.

1004

1005

1006 Table 7. Dimensions of LUT for the AEH algorithm using OMI.

Variable name	No. of Entries	Entries
SZA	7	0, 10, 20, 30, 40, 50, 60 degrees
VZA	7	0, 10, 20, 30, 40, 50, 60 degrees
RAA	10	0, 20, 40, 60, 80, 100, 120, 140, 160, 180 degrees
AOD	13	0.0, 0.2, 0.4, 0.6, 0.8, 1.0, 1.3, 1.6, 1.9, 2.2, 2.5, 3.0, 5.0
AEH	16	0.0, 1.0, 1.2, 1.4, 1.6, 1.8, 2.0, 2.2, 2.4, 2.6, 2.8, 3.0, 3.5, 4.0, 5.0, 10.0 km
Aerosol Model	3	Dust, Carbonaceous, Non-absorbing [Climatology over East Asia site of AERONET]

1007

1008 Table 8. List of aerosol transport cases and its period for comparison.

Case	Period
1	March, 28, 2007 - April, 2, 2007
2	May, 5, 2007 - May, 10, 2007
3	May, 25, 2007 - May, 26, 2007
4	February, 19, 2008 - February, 21, 2008
5	April, 3, 2008 - April, 5, 2008
6	May, 28, 2008 - May, 31, 2008
7	December, 4, 2008 - December, 7, 2008

1009

Figures

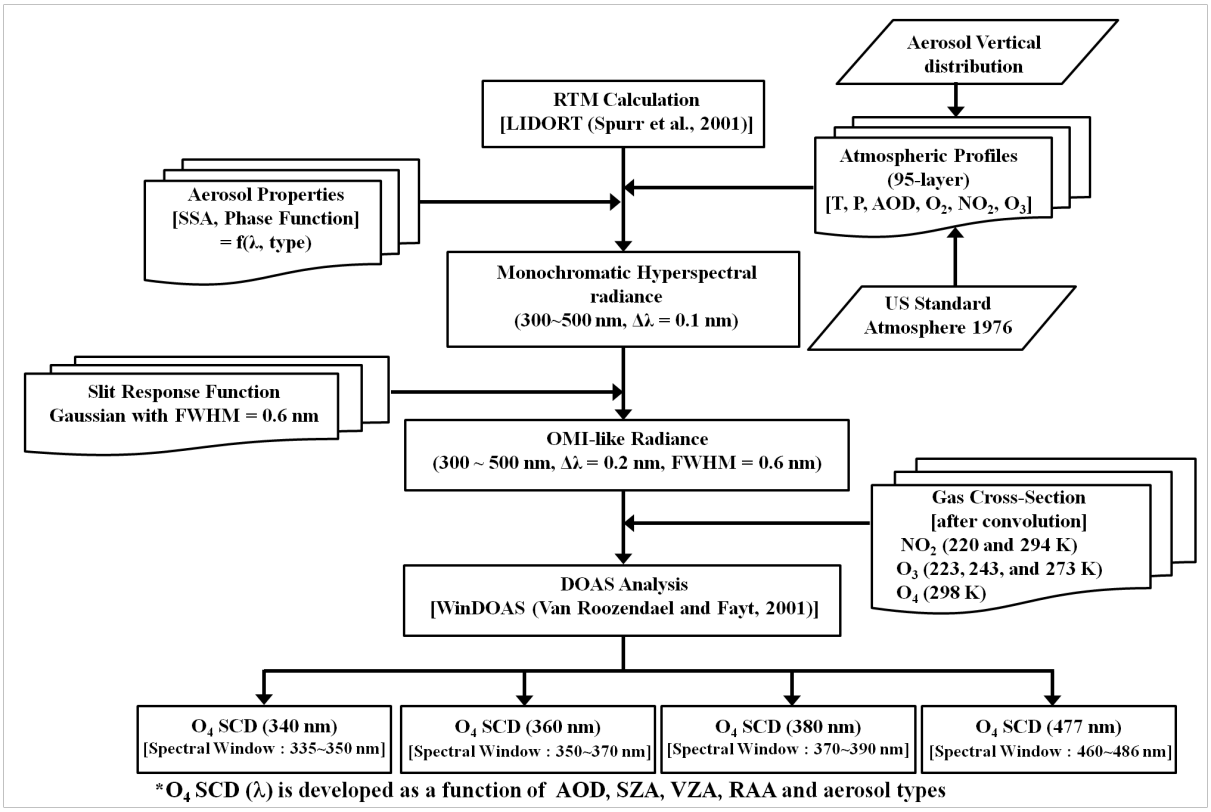

Figure 1. Flowchart of the simulated O_4 SCD estimation.

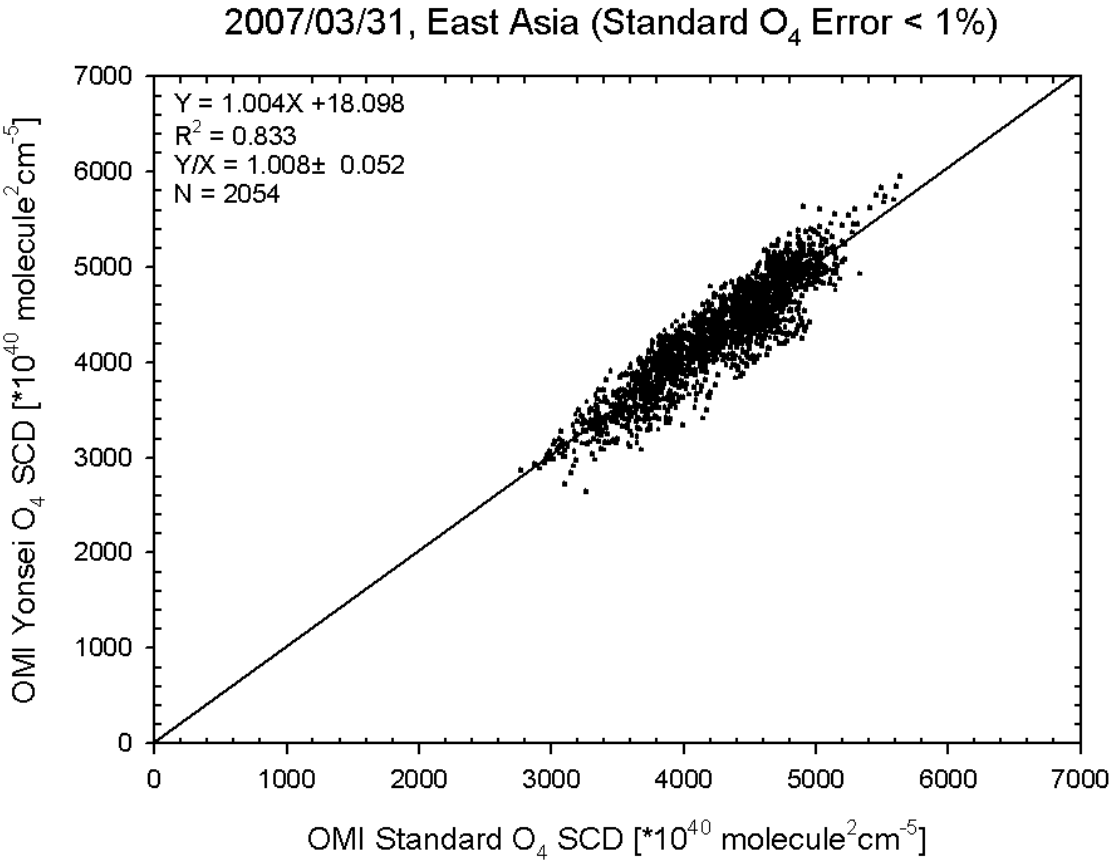

Figure 2. Comparison of O_4 SCD with the OMI standard product and directly retrieved from OMI radiance on March 31, 2007.

(a)

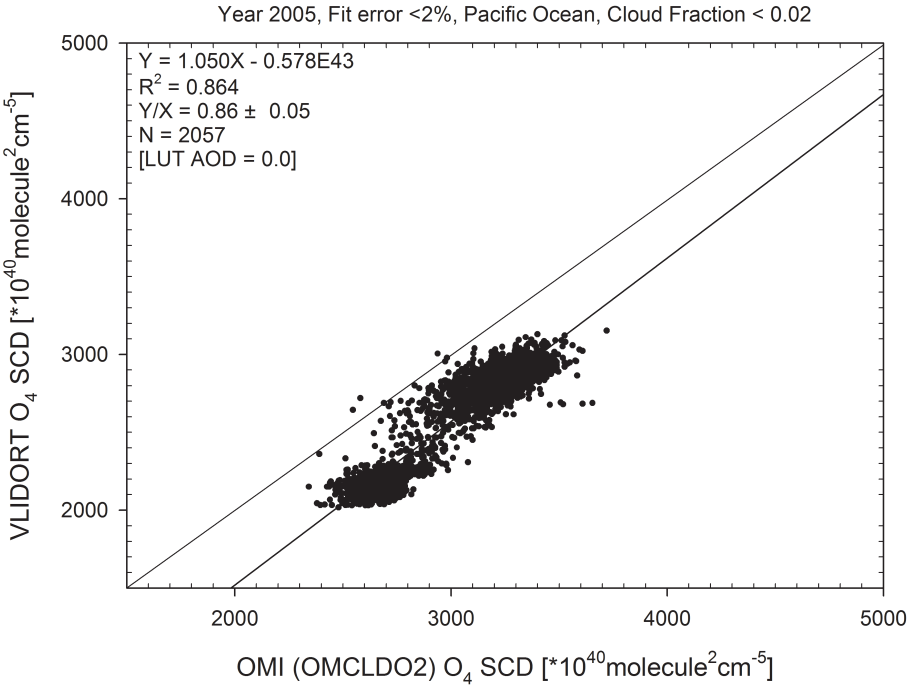

(b)

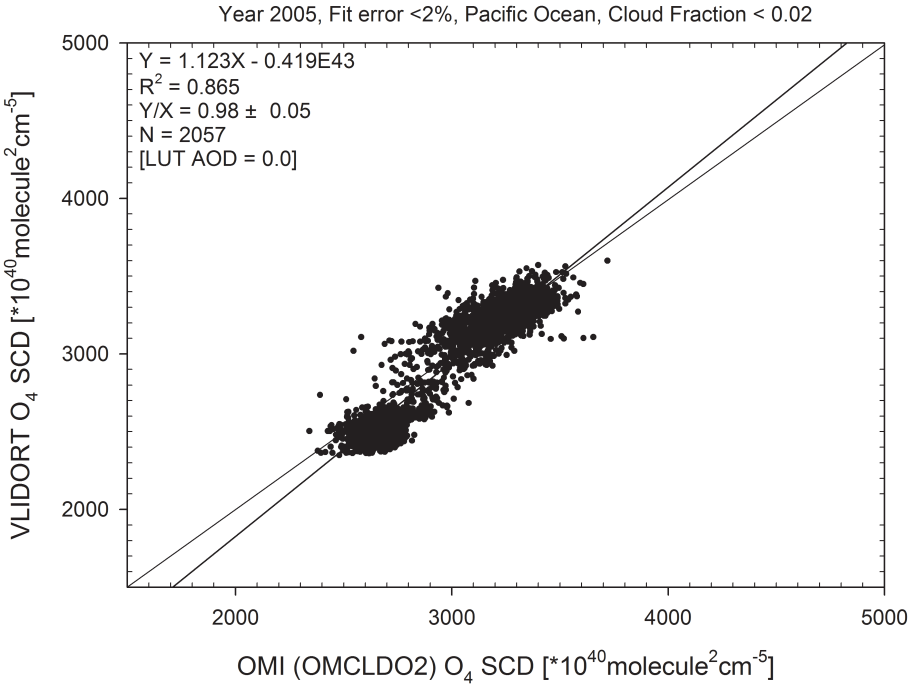

Figure 3. Comparison of the O_4 SCD at 477 nm between the standard product from OMI and calculated value from LUT (a) before and (b) after correction of LER.

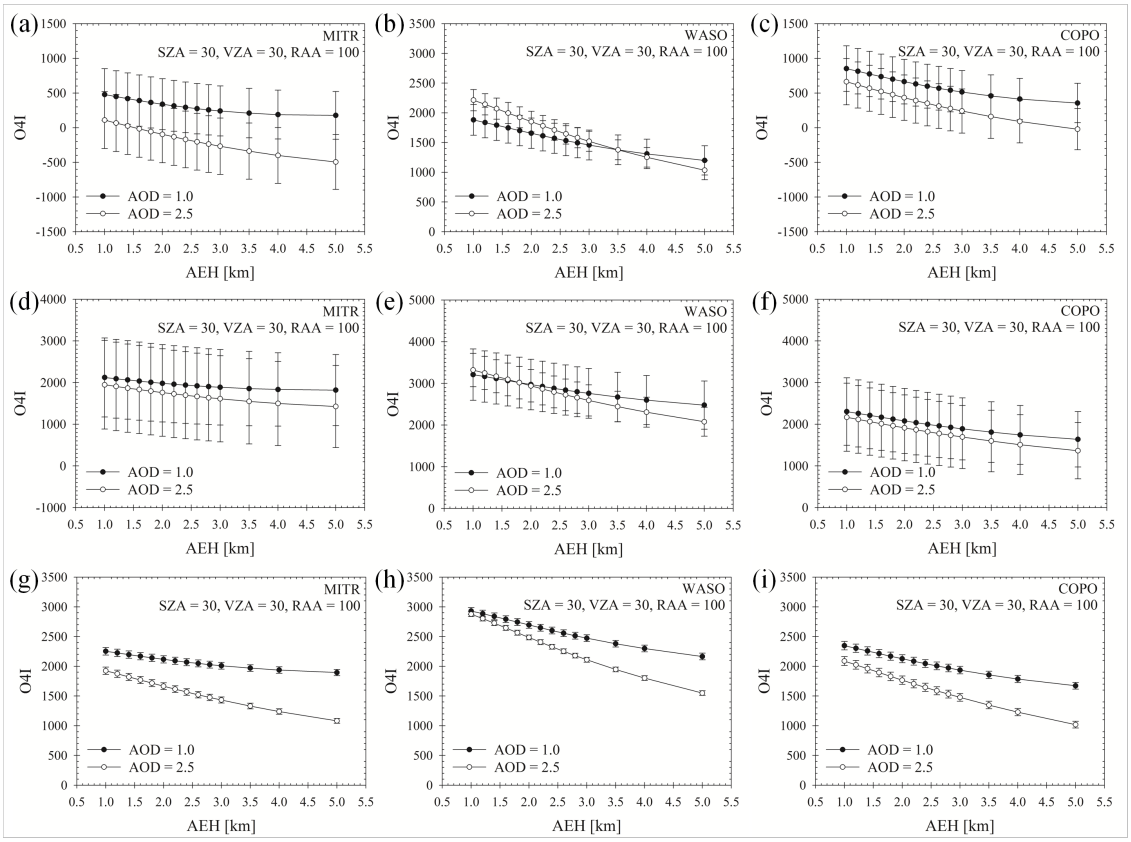

Figure 4. The O4I at 360 nm band for (a) MITR, (b) WASO, and (c) COPO, (d) at 380 nm band for MITR, (e) WASO, and (f) COPO, and (g) at 477 nm band for MITR, (h) WASO, and (i) COPO as a function of AEH.

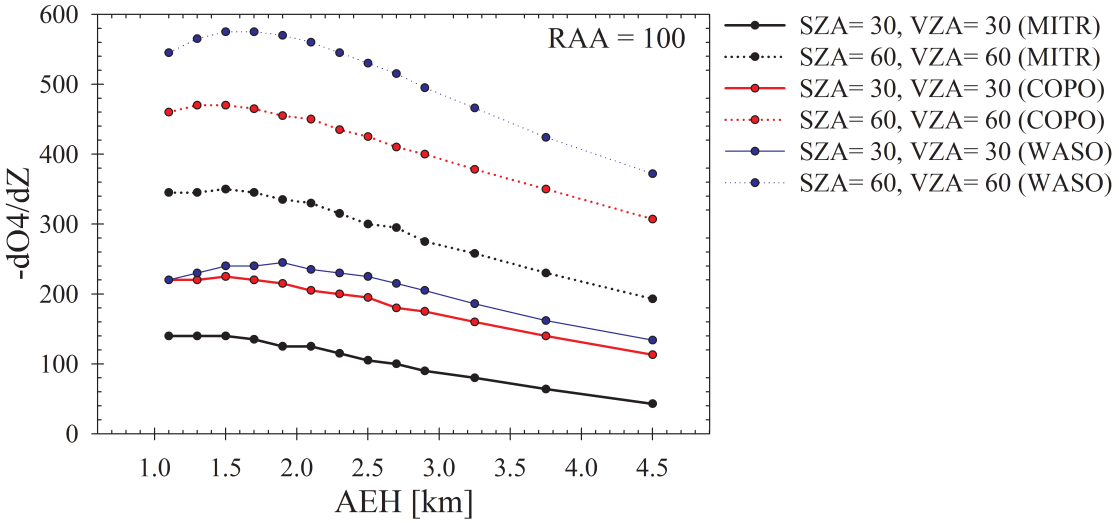

Figure 5. The AEH sensitivity to O4I (-dO4/dZ) with changing observation geometries at 477 nm.

(a)

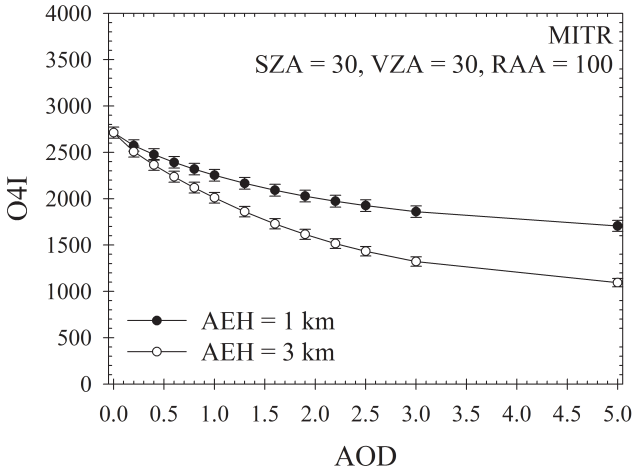

(b)

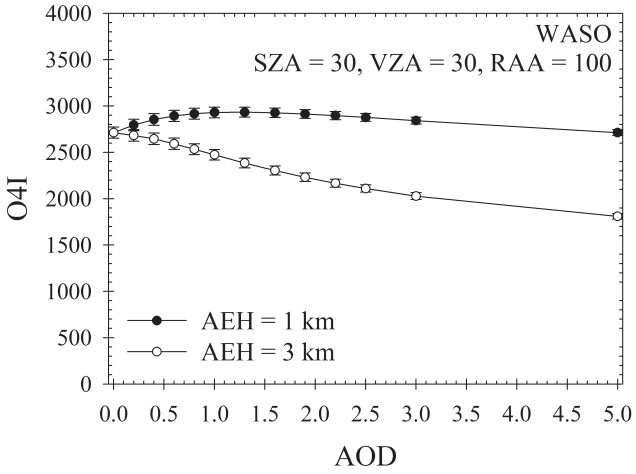

(c)

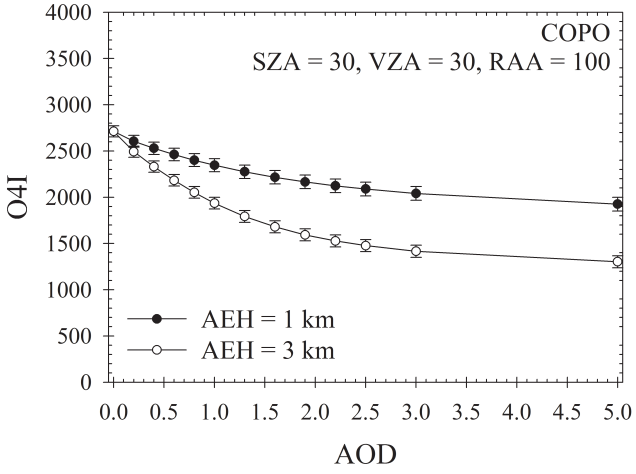

Figure 6. The O4I of (a) MITR, (b) WASO, and (c) COPO types as a function of AOD.

(a)

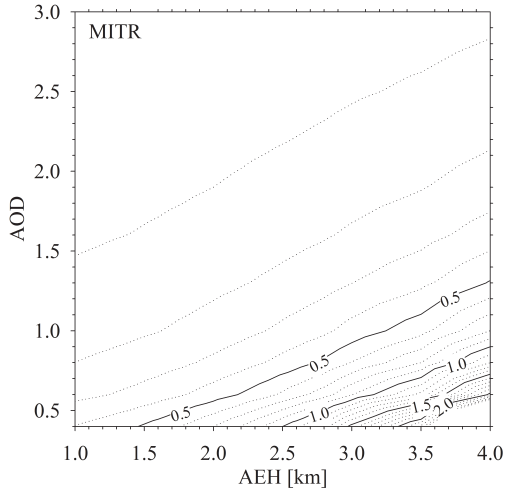

(b)

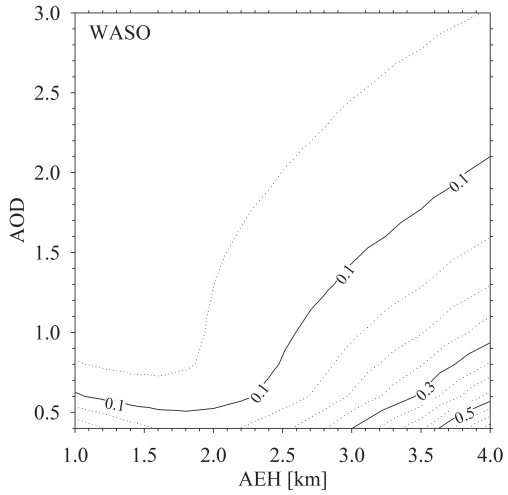

(c)

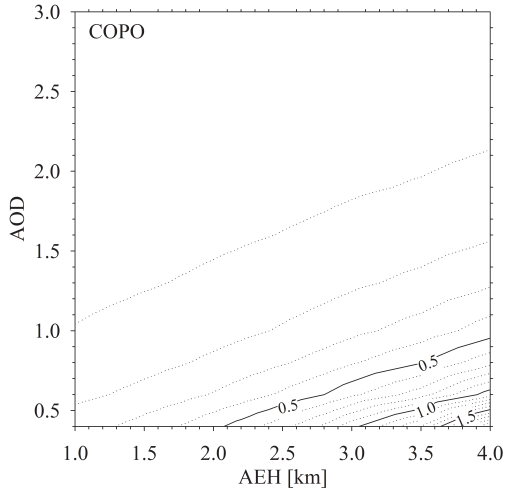

Figure 7. AEH error of (a) MITR, (b) WASO, and (c) COPO for AOD difference of 0.1 as a function of reference AEH and AOD.

(a)

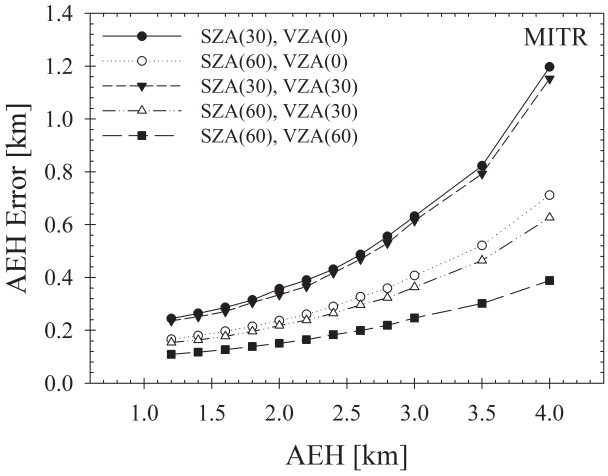

(b)

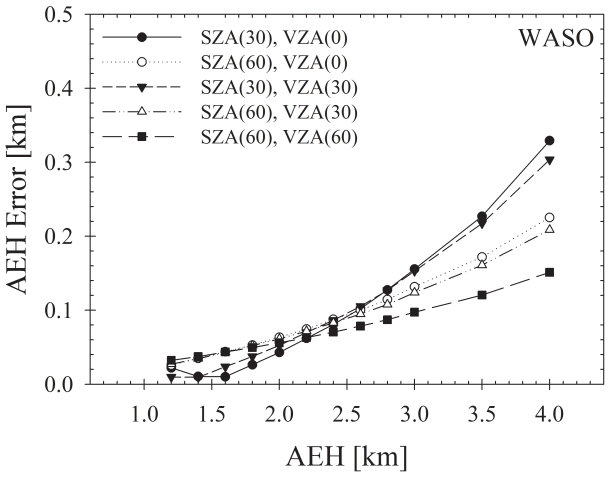

(c)

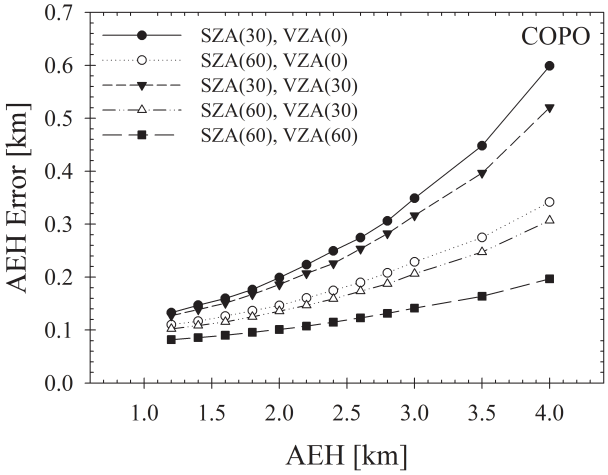

Figure 8. AEH error of (a) MITR, (b) WASO, and (c) COPO for AOD difference of 0.1 as changing viewing geometries.

(a)

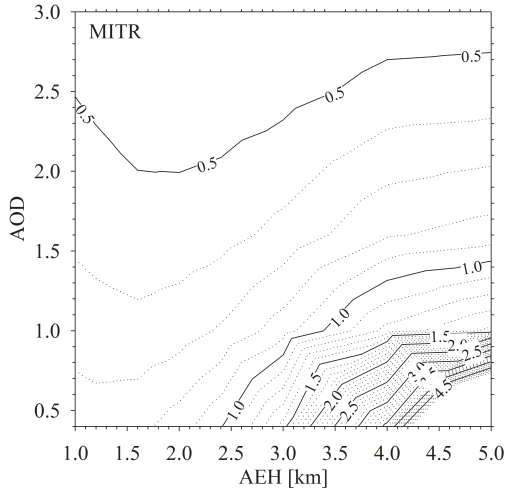

(b)

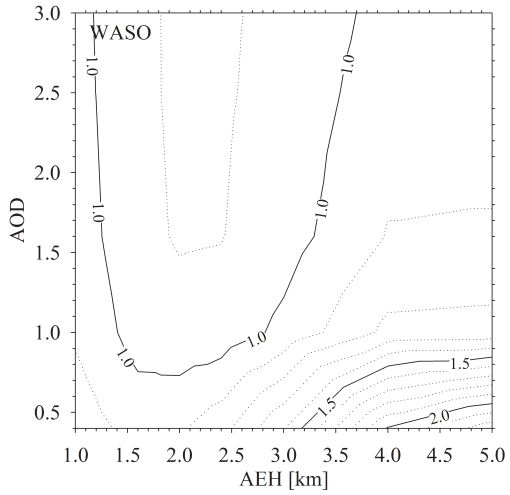

(c)

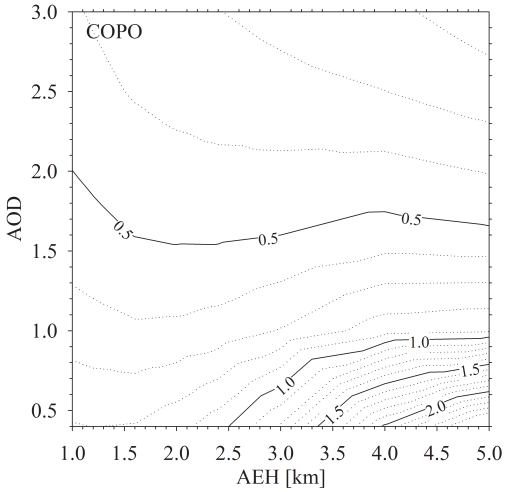

Figure 9. Same as Figure 7 except for SSA difference of 10%.

(a)

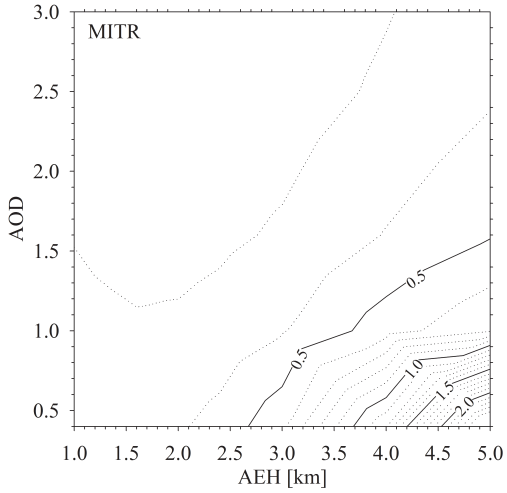

(b)

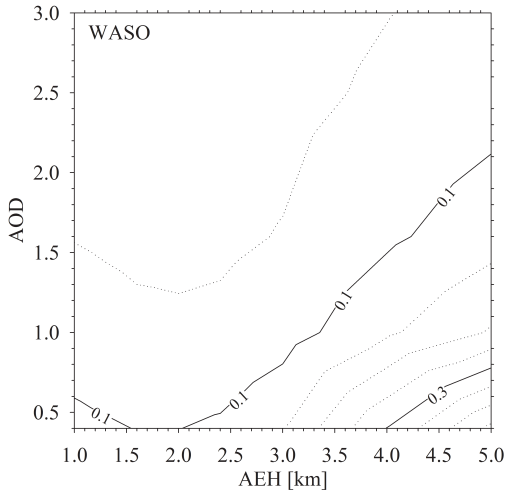

(c)

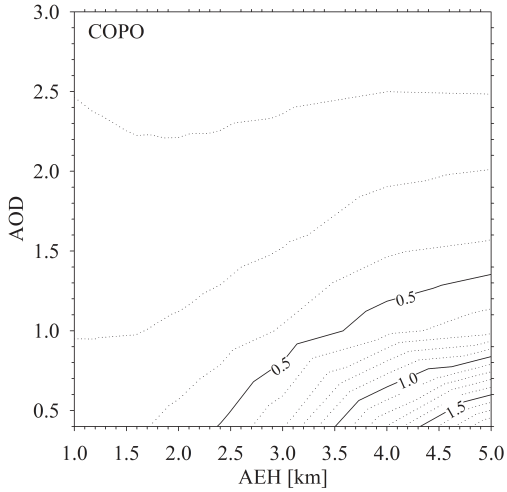

Figure 10. Same as Figure 7 except for particle size difference of 20%.

(a)

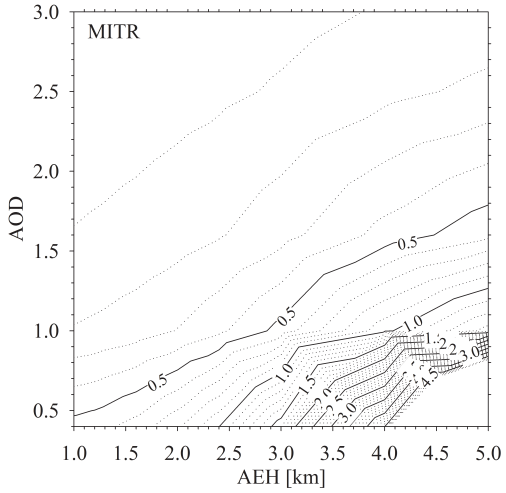

(b)

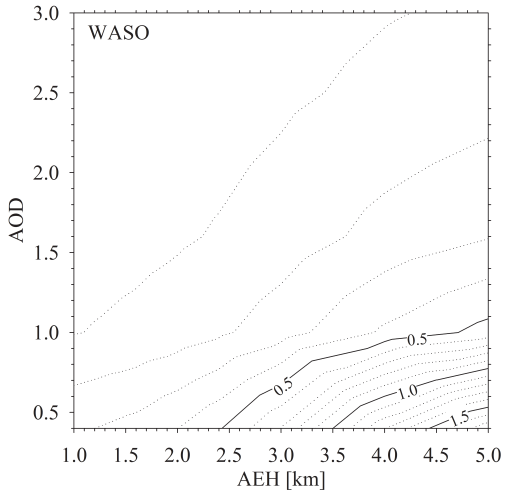

(c)

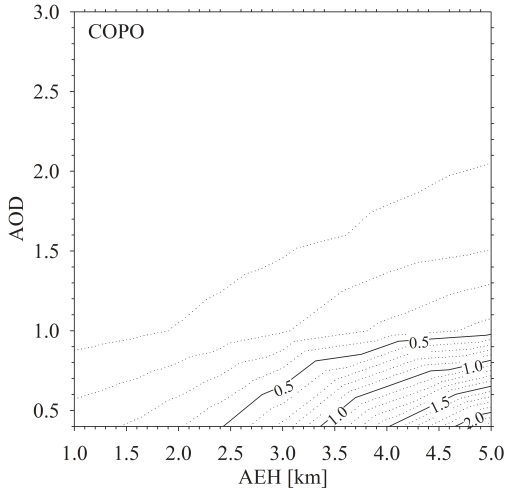

Figure 11. Same as Figure 7 except for surface albedo difference of 0.02.

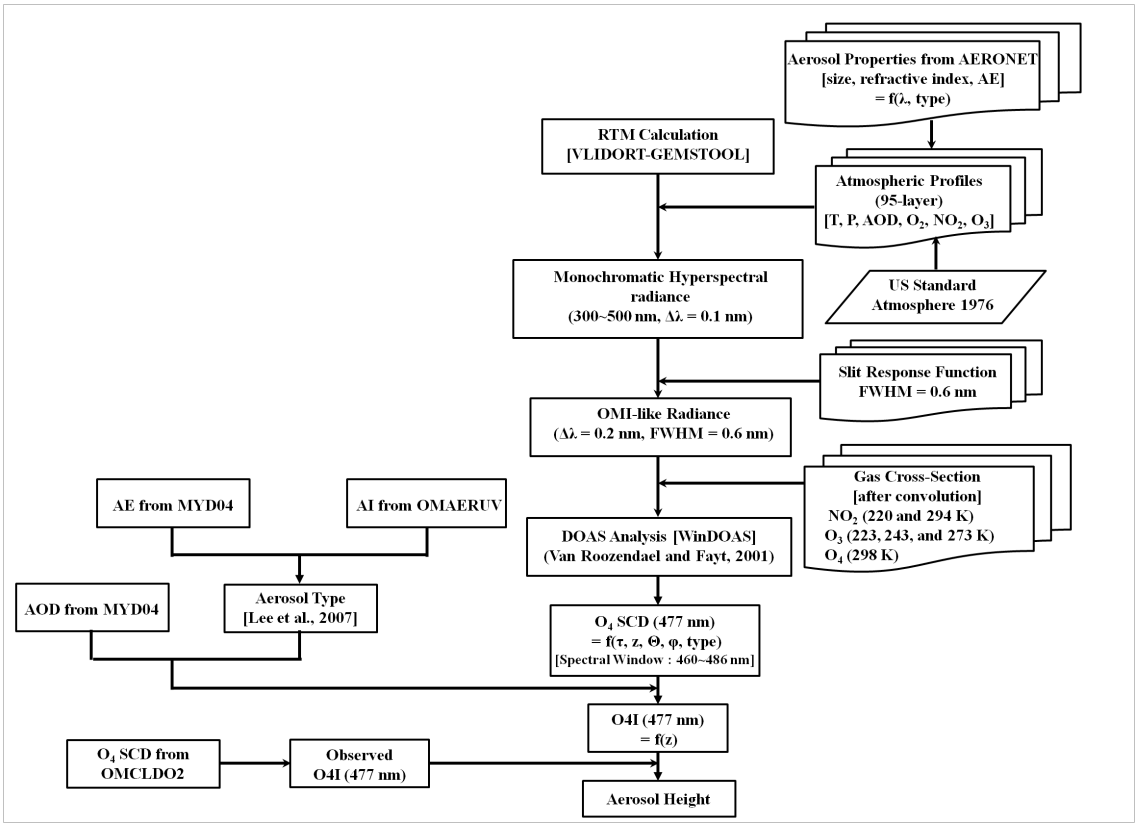

Figure 12. Flowchart of the retrieval algorithm for AEH from OMI observation.

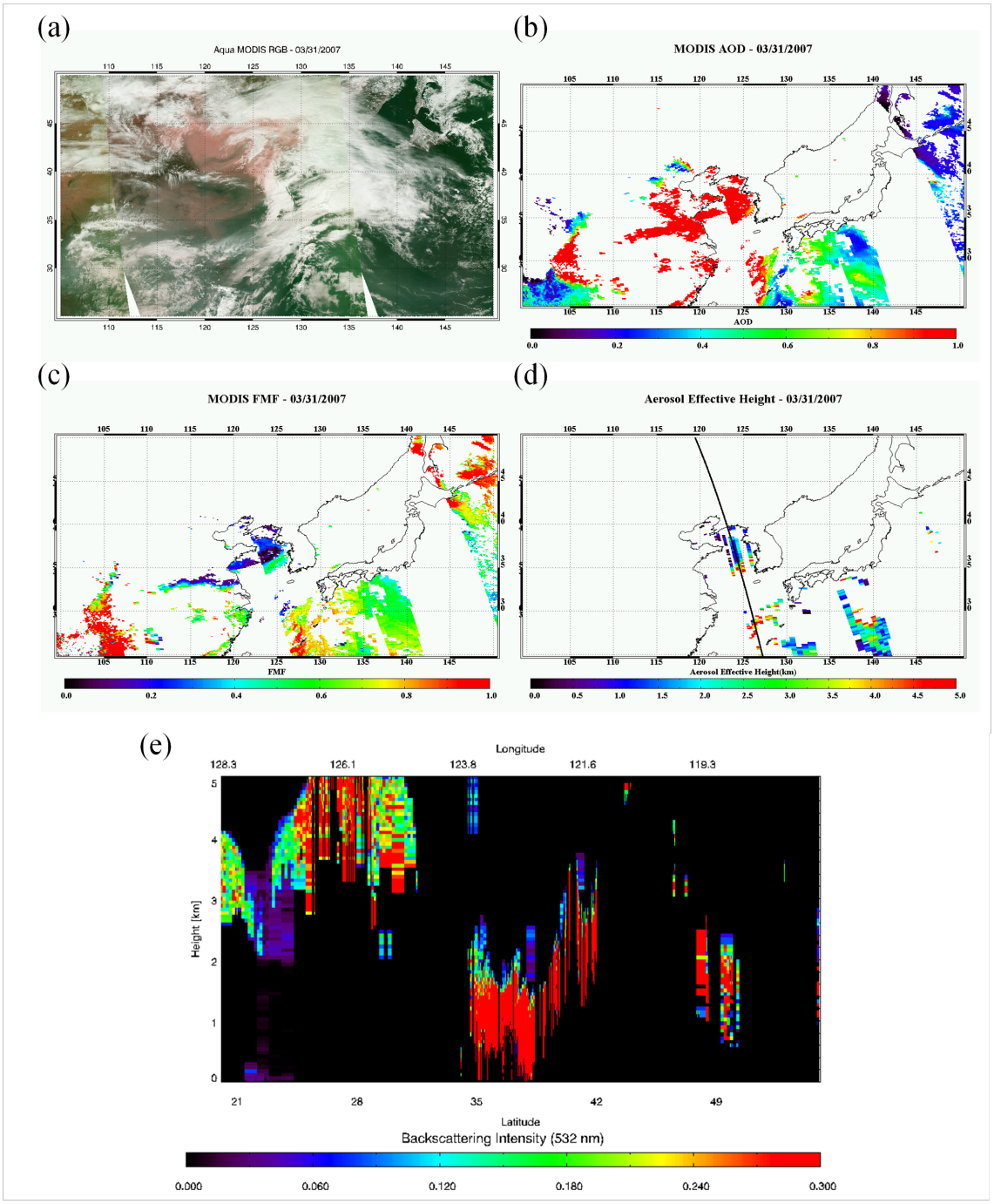

Figure 13. (a) MODIS RGB, (b) AOD, (c) FMF, (d) and AEH distribution from OMI over East Asia, and (e) backscattering Intensity at 532 nm from CALIOP observation over Yellow Sea on March 31, 2007.

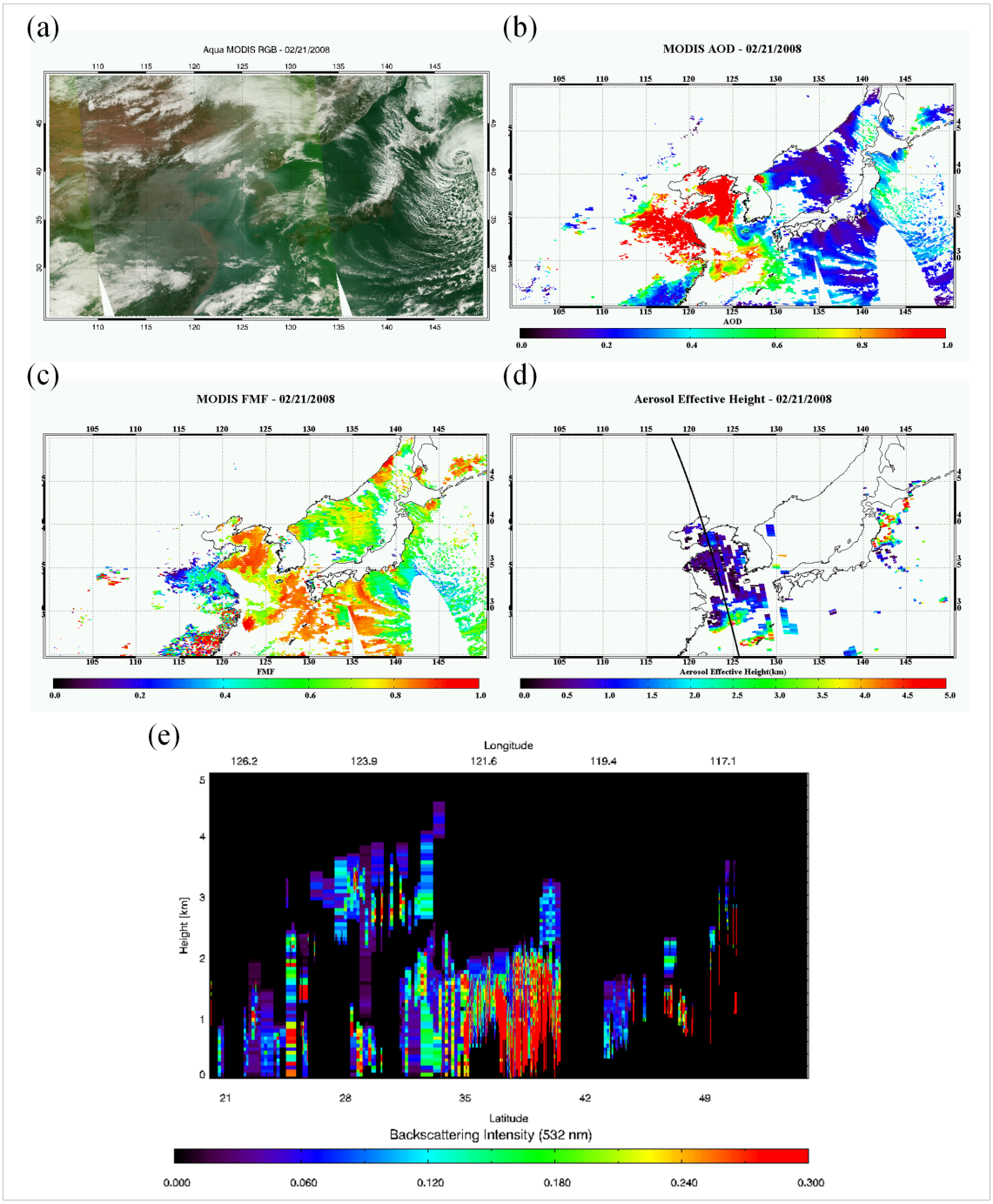

Figure 14. (a) MODIS RGB, (b) AOD, (c) FMF, (d) and AEH distribution from OMI over East Asia, and (e) backscattering Intensity at 532 nm from CALIOP observation over coastal region of China on February 21, 2008.

(a)

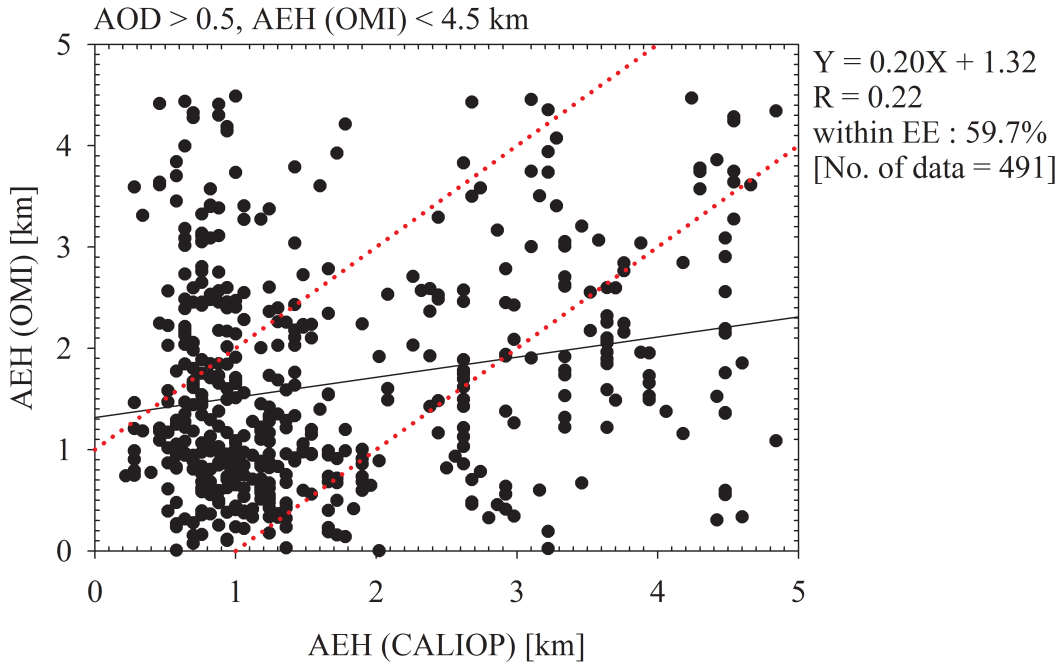

(b)

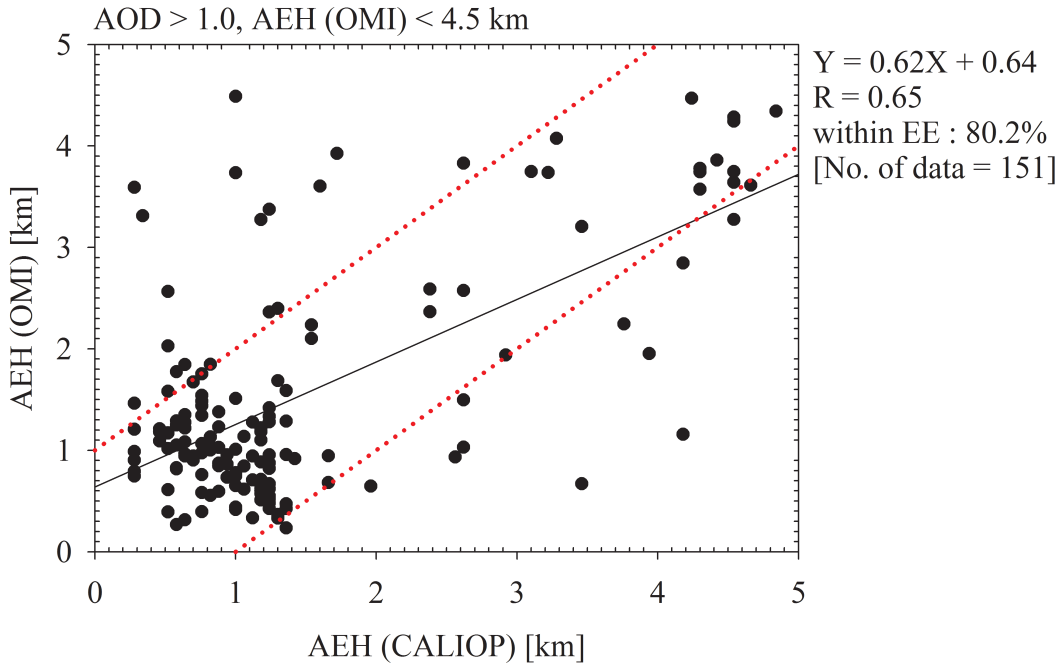

Figure 15. Comparison of AEH with CALIOP and OMI as (a) AOD > 0.5, and (b) AOD > 1.0 on aerosol transport cases in 2007 and 2008 over East Asia.